applied sciences

MDPI

Article

Optimal Design and Tuning of Novel Proportional Integral Derivative with Filter Thyristor-Controlled Series Compensator Stabiliser Using a New Hybrid Technique

Abdul Waheed Khawaja [1,2,*], Nor Azwan Mohamed Kamari [1,*], Muhammad Ammirrul Atiqi Mohd Zainuri [1], Mohd Asyraf Zulkifley [1], Mohd Hairi Mohd Zaman [1] and Ismail Musirin [3]

[1] Department of Electrical, Electronic & System Engineering, Faculty of Engineering and Built Environment, Universiti Kebangsaan Malaysia, Bangi 43600, Malaysia
[2] Department of Electrical Engineering, Faculty of Engineering & Technology, Bahauddin Zakariya University, Multan 60800, Pakistan
[3] School of Electrical Engineering, College of Engineering, Universiti Teknologi MARA, Shah Alam 40450, Malaysia
* Correspondence: khawaja@bzu.edu.pk (A.W.K.); azwank@ukm.edu.my (N.A.M.K.)

Abstract: This paper proposes a novel robust thyristor-controlled series compensator (TCSC) controller based on proportional integral derivative with filter (PIDF) and uses a new hybrid optimisation evolutionary programming sine cosine algorithm (EPSCA) to improve the power system's angle stability. The problem of the PIDF-TCSC design is transformed into an optimisation problem based on performance indices, such as damping factor, damping ratio, and eigenvalues, where the multi-objective function is employed to obtain the optimal stabiliser parameters. To examine the robustness of PIDF-TCSC, it was tested on a single-machine infinite-bus power system under different operating conditions. The performance of the system with the PIDF-TCSC controller was compared with the simulation results, and the results obtained with the proposed EPSCA were compared with those obtained with SCA, moth flame optimisation, and EP-based PIDF-TCSC methods. Simulation results showed the effectiveness of EPSCA for the PIDF-TCSC design and the superior robust performance for the enhancement of power system stability compared with other techniques in different cases.

Keywords: angle stability; objective function; eigenvalue analysis; TCSC; PIDF; optimisation

check for updates

Citation: Khawaja, A.W.; Kamari, N.A.M.; Zainuri, M.A.A.M.; Zulkifley, M.A.; Zaman, M.H.M.; Musirin, I. Optimal Design and Tuning of Novel Proportional Integral Derivative with Filter Thyristor-Controlled Series Compensator Stabiliser Using a New Hybrid Technique. *Appl. Sci.* **2022**, *12*, 11153. https://doi.org/10.3390/app122111153

Academic Editor: César M. A. Vasques

Received: 27 September 2022
Accepted: 20 October 2022
Published: 3 November 2022

Publisher's Note: MDPI stays neutral with regard to jurisdictional claims in published maps and institutional affiliations.

Copyright: © 2022 by the authors. Licensee MDPI, Basel, Switzerland. This article is an open access article distributed under the terms and conditions of the Creative Commons Attribution (CC BY) license (https://creativecommons.org/licenses/by/4.0/).

1. Introduction

Demands from the environment and the economy have driven power networks to become much more heavily laden and inadequately dampened. With the rise in electric power consumption and the need to regulate the system quickly and adaptably in a competitive context, current power systems can now survive challenging conditions. However, unanticipated disturbances cause poorly damped oscillations that eventually lead to instability, which have become more common in electrical power networks all over the world. A power system must be able to sustain operational stability under typical operating conditions and return to a suitable equilibrium following disturbances. Proper system modelling and damping controller devices are required to reduce oscillations and improve and maintain the angle stability of a power system. Coordination control, flexible alternating current transmission system (FACTS), and PSS are the three categories of dampening techniques that have been used. FACTS may provide damping for inter-area modes and for local-area oscillation modes [1–5].

High-power electronic technology-based superior control in high-voltage power transmission systems is used to reinforce power systems via FACTS technology, which has been

deployed in a significant number of real power systems. The following describes the active power delivered to the load via the transmission line:

$$P_{ab} = \frac{V_a V_b}{x_t} \sin\theta \quad (1)$$

where the θ is the phase angle between a transmission line's sending V_a and receiving V_b end voltages. Through the adjustment of line parameters, including line voltage, phase angle, and line impedance x_t, a FACTS device controller can manage the flow of electricity down a transmission line.

Thyristor-based and convertor-based FACTS controllers can be distinguished by their base. The three main categories of thyristor-based controllers are static var compensators (SVCs), which regulate line voltage magnitude; thyristor-controlled series compensators (TCSCs), which regulate line impedance to regulate power flow; and thyristor-controlled phase shifters (TCPSs), which regulate the line voltage phase angle to regulate power flow. Two different types of converter-based FACTS controllers exist, namely, the voltage source converter (VSC), which is built on synchronous voltage sources that act as an ideal machine with no rotation and inertia, and the current source converter. Both devices generate and regulate reactive power flow independently of line voltages and currents. The static synchronous compensator (STATCOM), static synchronous series compensator (SSSC), and unified power flow controller (UPFC) are the three primary types of VSC-based FACTS controllers [2].

Using a FACTS has advantages such as power flow control, increased transmission and loading capacity, improved stability of the power system, secure tie line connections, voltage control and flicker mitigation, reactive power compensation, reduced reactive power flows, improved power quality and power conditioning, and flexibility in connecting new renewable and distributed generation [6].

The fundamental TCSC module, which consists of a series of fixed capacitor and a thyristor-controlled reactor (TCR), is a capacitive reactance controller in the power transmission system that ensures that reactive power is exchanged continuously and effectively to control the parameters of power lines. The TCSC uses an open-loop control system to adjust its series reactance and control the flow of power. By varying its reactance, the TCSC controls the line current through a closed loop. When functioning in an open or a closed loop, the TCSC provides power flow control or line current control by varying its reactance. By quickly changing the reactance of a transmission line, TCSC increases the system's capacity for power transfer, dampening, mitigation of sub-synchronous resonance, and voltage stability [2]. P_{ab} in line power flow is specified as

$$P_{ab} = \frac{V_a V_b}{x_t - x_c} \sin\delta \quad (2)$$

where x_c is the TCSC reactance, and x_t is the transmission line reactance.

In recent years, oscillations in power networks have been reduced by using a variety of FACTS devices to build controllers that inject or absorb reactive power. Two FACTS shunt devices—SVC and STATCOM—have been used for dampening to increase the angle stability of FACTS [7,8]. SVC is best used in the middle of transmission lines or at the sending end, as well as at buses and branches, and has applications in wind energy with a focus on high voltage drops. SVC is not permitted on PV buses [9]. STATCOM offers a stability buffer for transients and a single power factor for wind power systems. A damping performance analysis UPFC [10], which is a dynamic control technique to promote low-voltage ride-through capability in power systems [11], is also described in the literature. The UPFC is a multipurpose device that controls bus voltage; transmission line impedance, phase angle, line active, and reactive power flow; and bus impedance. To reduce local and intermode oscillations in power systems [9], PSS and FACTS devices with efficient controller coordination have been incorporated. The TCSC and SVC with PSS coordination control design are discussed in [12,13]. The optimal reactive power injection is used in the

TCSC model, which also has variable reactance. It is not compatible with transformer use at branches [9]. Furthermore, STATCOM, a UPFC, and an IPFC have coordinated PSS [14–16].

The design of damping controllers has been studied by a number of researchers. Some authors have taken into account lead lag controllers, and proportional integral (PI) and proportional integral derivative (PID) with various formulations of the objective function for stability analysis of the single machine infinite bus (SMIB) system [17–26]. The proportional integral derivative with filter (PIDF) is used to control the load frequency of a deregulated power system and to mitigate reactive losses in multi-phase flow regimes in pipelines and risers at offshore oilfields [27], buck converters for DC–DC converters, and industrial processes to obtain a true solution for high-level process oscillation [28] and to compensate for the reactive power for steady state and the transient stability of power systems [29].

To improve the efficiency of a hybrid microgrid system, a fuzzy PIDF load frequency controller was optimised using the marine predator algorithm [30]. The installation of a controller utilising the proper formulation may result in a damping scheme that contributes a sufficient amount. A suitable formulation of the objective function and a suitable damping scheme are essential for the robust design of the damping controller. To improve the stability of the SMIB system and the multimachine power system, an optimum optimisation technique needs to be found to create an objective function by comparing the performances of various formulations of objective functions.

In recent years, the use of heuristic algorithms as optimisation techniques to build damping controllers for the stability of power systems has become widespread and well recognised [18,31,32]. Many conventional heuristic algorithms have been used in research, and their performance is application focused. These heuristic algorithms are used extensively in SMIB systems and small multimachine power systems to construct damping controllers. Optimisation parameters have been reduced in many studies to reduce design complexity. However, examining the variance in design performance caused by the addition of more problem dimensions and all-optimisation parameters is crucial. The path of convergence is altered each time using a heuristic algorithm, which finds solutions through trial and error using stochastic approaches. Comparing the performance of algorithms when authors utilise a single convergence curve to test the performance of damping controllers in some instances is inappropriate. These issues are clear indicators that a thorough analysis was not performed before designing the damping controller for the power system. Designing a damping controller is a multimodal optimisation issue, and when the optimisation parameters in large power systems are increased, so are the complexity levels. These are intricate and challenging issues. Therefore, the performance of heuristic algorithms is negatively impacted by their ability to be trapped in the local minima. Heuristic algorithms thus become stuck in the local minima and perform worse as the issue dimension grows. As a result, developing a robust damping controller using an optimal damping scheme is challenging.

To find the best damping controller solution, exploration and exploitation processes must be balanced. Numerous metaheuristic optimisation algorithms have used stochastic techniques; yet these techniques have poor solution convergence. Several suggested approaches offer good search space exploration but have limited exploitation, or vice versa [22]. To locate the maxima or minima, metaheuristic optimisation techniques are employed. These methods either use algorithms based on swarms or evolution. Particle swarm optimisation (PSO), firefly, ant colony, gravitational search algorithm (GSA), and immunity algorithm (IA) are examples of swarm-based algorithms. The evolutionary programming (EP) differential algorithm, EP, and genetic algorithm (GA) are examples of evolution-based algorithms. Premature convergence is a constraint of GA and PSO brought on by the local minimum stagnation issue. GSA is limited in its ability to solve challenging optimisation issues. To find the best options for a damping controller, IA performs better during the exploration phase than during the exploitation phase. EP functions more effectively during the exploitation phase than during the exploration phase.

Other optimisation methods, such as tabu search and simulated annealing methods, have poor convergence rates and cannot handle multimodal issues [5,22].

Recently, a wide variety of indicators has been applied in the construction of controllers that inject or absorb reactive power to reduce oscillations in power networks. To reduce overshoots and settling times in power system oscillations, the following parameters are used: damping factor, damping ratio, eigenvalues, integral absolute error (IAE), integral squared error (ISE), integral of the time-weighted absolute error (ITAE), and integral of time multiplied by the squared error (ITSE). Damping ratio eigenvalue analysis provides the small-signal stability analysis for the two-area interconnected power system with load frequency controller in collaboration with FACTS and energy storage device [33]. ISE, ITSE, and power system stabilisers for improving dynamic stability [34,35] are used to more accurately assess the system performance for compensating reactive power [36]. In a deregulated environment, ITAE is used as the objective function for improving the stability of the power system based on a conventional UPFC and multi-source power system [28,37]. When evaluating the system's effectiveness for reactive power adjustment, the ITSE and damping ratio are used [38]. Overshoots of oscillations are mitigated by the damping ratio indicator. However, it performs poorly in terms of settling time, and conversely for the indicator of damping factor. Therefore, a single indicator cannot perform better in terms of both settling time and oscillation overshoots.

The key contributions of the paper are as follows:

- Novel mathematical modelling of a PIDF controller and its power stability aspect was used as a damping controller. This controller has never been applied to the stability of a power system.
- To build a reliable damping controller design for an SMIB system, the evolutionary programming sine cosine algorithm (EPSCA) technique was developed.
- A novel multi-objective (MO) function was created that incorporates a strong damping controller architecture for SMIB systems and may be used in large power systems.
- The proposed EPSCA is validated with the standard SCA, MFO, and EP techniques.

The modelling of an SMIB power system installed with a TCSC, a TCSC SMIB system installed with PIDF controller, and a proposed multi objective function is described in Section 2. Section 3 describes the proposed EPSCA, SCA, MFO, and EP algorithms. The results of simulations of four different loading condition scenarios are represented in Section 4. Section 5 presents the discussion section. Finally, Section 6 condenses the conclusions.

2. Materials and Methods

The FACTS has become a standard, effective, and economical device installed in long transmission lines to increase the damping of power system oscillations. The cause of inter-area oscillations is the absence of a power plant closes to the tie line and long-distance power transmission lines in a large, interconnected power system. Hence, a FACTS-based stabiliser is an option to supply sufficient damping to inter-area oscillations in large, interconnected power systems [17,39,40].

2.1. Modelling of SMIB Power System Installed with a TCSC

The SMIB power system with a TCSC, which is employed for stability purposes, is depicted in Figure 1. A synchronous generator G is shown in Figure 1 with an excitation system, terminal voltage V_t, and a TCSC damping controller connected to an infinite bus with voltage V_b through transmission lines of impedance x_t, where R_E and X_E are real and imaginary parts, respectively, and x_{tcsc} stands for TCSC variable reactance. With the use of this figure, TCSC damping controllers are designed [2].

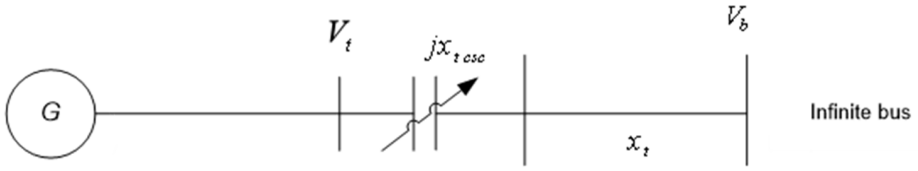


Figure 1. Single-machine infinite-bus power system installed with a TCSC.

The simplified model of a single-machine infinite-bus system installed with TCSC is as follows:

$$\dot{\delta} = \omega_o(\omega - 1) \tag{3}$$

$$\dot{\omega} = [P_m - P_t - \mathrm{D}(\omega - 1)]/\mathrm{M} \tag{4}$$

$$\dot{\acute{E}}_q = [-E_q + E_{fd}]/\acute{T}_{do} \tag{5}$$

$$\dot{E}_{fd} = -\frac{E_{fd}}{T_A} + \frac{K_A}{T_A}[V_{tref} - V_t] \tag{6}$$

where

$$P_t = \frac{\acute{E}_q V_b}{(\acute{x}_d + x_t - x_{tcsc})} \sin\delta - \frac{V_b^2}{2}(x_q - \acute{x}_d)\frac{\sin 2\delta}{(\acute{x}_d + x_t - x_{tcsc})(x_q + x_L - x_{tcsc})} \tag{7}$$

$$E_q = \frac{\acute{E}_q(x_d + x_L - x_{tcsc})}{(\acute{x}_d + x_t - x_{tcsc})} - \frac{(x_d - \acute{x}_d)V_b \cos\delta}{(\acute{x}_d + x_t - x_{tcsc})} \tag{8}$$

$$E_{fd} = E_{fdo} + E_{fd} \tag{9}$$

$$v_{td} = \frac{x_q V_b \sin\delta}{(x_q + x_L - x_{tcsc})} \tag{10}$$

$$v_{tq} = \frac{\acute{x}_d V_b \cos\delta}{(\acute{x}_d + x_t - x_{tcsc})} + \frac{\acute{E}_q x_t}{(\acute{x}_d + x_t - x_{tcsc})} \tag{11}$$

$$V_t = \sqrt{v_{td}^2 + v_{tq}^2} \tag{12}$$

By linearising Equations (3)–(12), we have

$$\Delta P_t = K_1\Delta\delta + K_2\acute{E}_q + K_p\Delta x_{tcsc} \tag{13}$$

$$\Delta E_q = K_4\Delta\delta + K_3\acute{E}_q + K_q\Delta x_{tcsc} \tag{14}$$

$$\Delta V_t = K_5\Delta\delta + K_6\acute{E}_q + K_v\Delta x_{tcsc} \tag{15}$$

where

$$K_1 = \frac{\acute{E}_{qo} V_b \cos\delta_o}{(\acute{x}_d + x_t - x_{tcsc})} - \frac{V_b^2(x_q - \acute{x}_d)\cos 2\delta_o}{(\acute{x}_d + x_t - x_{tcsc})(x_q + x_L - x_{tcsc})} \tag{16}$$

$$K_2 = \frac{V_b \sin\delta_o}{(\acute{x}_d + x_t - x_{tcsc})} \tag{17}$$

$$K_3 = \frac{(x_d + x_L - x_{tcsc})}{(\acute{x}_d + x_t - x_{tcsc})} \tag{18}$$

$$K_4 = (x_d - \acute{x}_d)K_2 \tag{19}$$

$$K_5 = \frac{V_b cos\delta_o x_q v_{tdo}}{V_{to}(x_q + x_L - x_{tcsc})} - \frac{v_{tqo}\acute{x}_d V_b sin\delta_o}{V_{to}(\acute{x}_d + x_t - x_{tcsc})} \tag{20}$$

$$K_6 = \frac{v_{tqo}(x_L - x_{tcsc})}{V_{to}(\acute{x}_d + x_t - x_{tcsc})} \tag{21}$$

$$K_p = \frac{\acute{E}_{qo} V_b \sin\delta_o}{(\acute{x}_d + x_t - x_{tcsc})^2} - \frac{V_b^2 (x_q - \acute{x}_d)((\acute{x}_d + x_t - x_{tcsc}) + (x_q + x_L - x_{tcsc}))\ \sin 2\delta_o}{2(\acute{x}_d + x_t - x_{tcsc})^2 (x_q + x_L - x_{tcsc})^2} \tag{22}$$

$$K_q = \frac{\acute{E}_{qo}(x_d + x_L - x_{tcsc})}{(\acute{x}_d + x_t - x_{tcsc})^2} - \frac{(x_d - \acute{x}_d) V_b \cos\delta_o}{(\acute{x}_d + x_t - x_{tcsc})^2} \tag{23}$$

$$K_v = \frac{v_{tdo} x_q V_b \sin\delta_o}{V_{to}(x_q + x_L - x_{tcsc})^2} + \frac{v_{tqo}}{V_{to}}\left[\left(\frac{x_L}{(\acute{x}_d + x_t - x_{tcsc})^2} - \frac{1}{(\acute{x}_d + x_t - x_{tcsc})}\right)\acute{E}_{qo} + \frac{\acute{x}_d V_b \cos\delta_o}{(\acute{x}_d + x_t - x_{tcsc})^2}\right] \tag{24}$$

The values of Equations (13)–(15) are placed in Equations (3)–(6). Hence, the Equations (25)–(28) are the extended Phillips–Heffron model of the single-machine infinite-bus power system installed with the TCSC stabiliser, which is shown in Figure 2.

$$\Delta\dot{\delta} = \omega_o \Delta\omega \tag{25}$$

$$\Delta\dot{\omega} = [-K_1\Delta\delta - \mathrm{D}\Delta\omega - K_2\Delta\acute{E}_q - K_p\Delta x_{tcsc}]/\mathrm{M} \tag{26}$$

$$\Delta\dot{\acute{E}}_q = [-K_4\Delta\delta - K_3\Delta\acute{E}_q - K_q\Delta x_{tcsc} + \Delta\acute{E}_{fd}]/\acute{T}_{do} \tag{27}$$

$$\Delta\dot{\acute{E}}_{fd} = -\frac{\Delta\acute{E}_{fd}}{T_A} - \frac{K_A}{T_A}[K_5\Delta\delta + K_6\Delta\acute{E}_q + K_v\Delta x_{tcsc}] \tag{28}$$

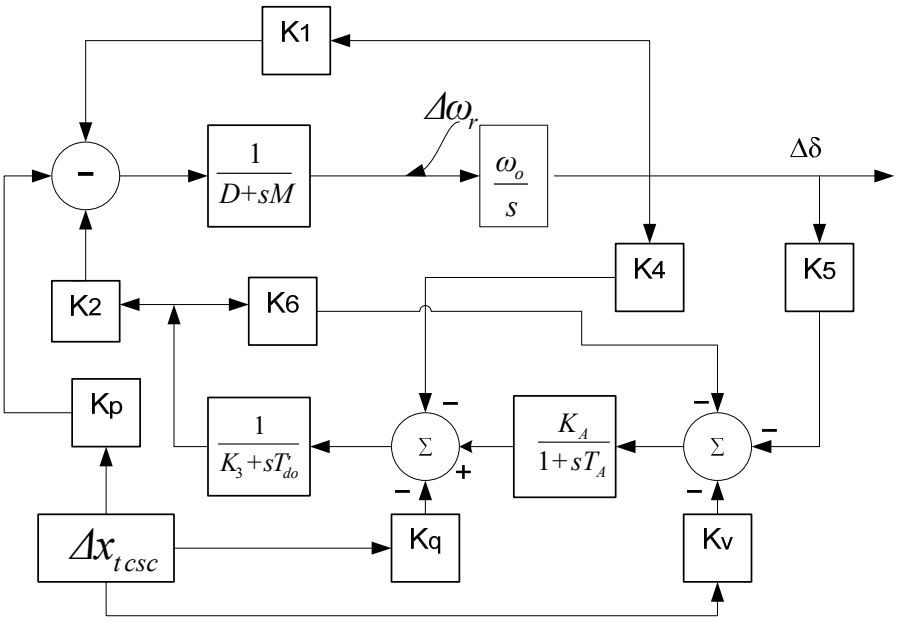


Figure 2. Extended Phillips–Heffron model of the single-machine infinite-bus power system installed with a TCSC stabiliser.

The system in Figure 2 expressed by a linearised state space mathematical model is represented as follows:

$$\dot{X} = A_{tcsc}.\mathrm{X} + B_{tcsc}.\mathrm{U} \tag{29}$$

$$\dot{X} = [\Delta\dot{\delta}\ \ \Delta\dot{\omega}\ \ \Delta\dot{\acute{E}}_q\ \ \Delta\dot{\acute{E}}_{fd}] \tag{30}$$

$$\mathrm{X} = [\Delta\delta\ \ \Delta\omega\ \ \Delta\acute{E}_q\ \ \Delta\acute{E}_{fd}] \tag{31}$$

$$A_{tcsc} = \begin{bmatrix} 0 & \omega_o & 0 & 0 \\ -\frac{K_1}{M} & -\frac{D}{M} & -\frac{K_2}{M} & 0 \\ -\frac{K_4}{T'_{do}} & 0 & -\frac{K_3}{T'_{do}} & \frac{1}{T'_{do}} \\ -\frac{K_A K_5}{T_A} & 0 & -\frac{K_A K_6}{T_A} & -\frac{1}{T_A} \end{bmatrix} \tag{32}$$

$$B_{tcsc} = \begin{bmatrix} 0 \\ -\frac{K_p}{M} \\ -\frac{K_q}{T'_{do}} \\ -\frac{K_A K_v}{T_A} \end{bmatrix} \tag{33}$$

$$U = [\Delta x_{tcsc}] \tag{34}$$

where M refers to the inertia of the rotor; δ and ω express the rotor angle position of the synchronous machine and speed, respectively; $\acute{E}_{fd}$ denotes the machine transient excitation voltage; $\acute{E}_q$ refers to the machine q-axis transient excitation voltage; K_A and T_A express the gain and time constant of the AVR, respectively; D represents the damping coefficient of rotor motion; $\acute{T}_{do}$ refers to the time constant of machine field winding; and the coefficient K_p and the coefficients K_q and K_v are the weight parameters that determine how much damping torque and synchronising torque are contributed by the TCSC stabiliser, respectively. K_1, K_2, and K_4 are machine constants, and K_3, K_5, and K_6 are the SMIB and excitation systems with AVR constants. x_d, $\acute{x}_d$, x_q and $\acute{x}_q$ are the d-axis reactance, transient d-axis reactance, q-axis reactance, and transient q-axis reactance of the field winding of the machine, respectively.

2.2. Modelling of a TCSC SMIB System Installed with PIDF Controller

The block diagram of the PIDF controller is shown in Figure 3. The transfer function of the PIDF controller with parameters K_P, K_D, K_I, and N in Figure 3 is given as

$$\Delta\sigma = (K_P + \frac{K_I}{s} + K_D \frac{Ns}{s+N})\Delta\omega \tag{35}$$

where K_P, K_D, K_I, and N are the proportional gain constant, derivative gain constant, integral gain constant, and derivative filter coefficient of the PIDF controller, respectively.

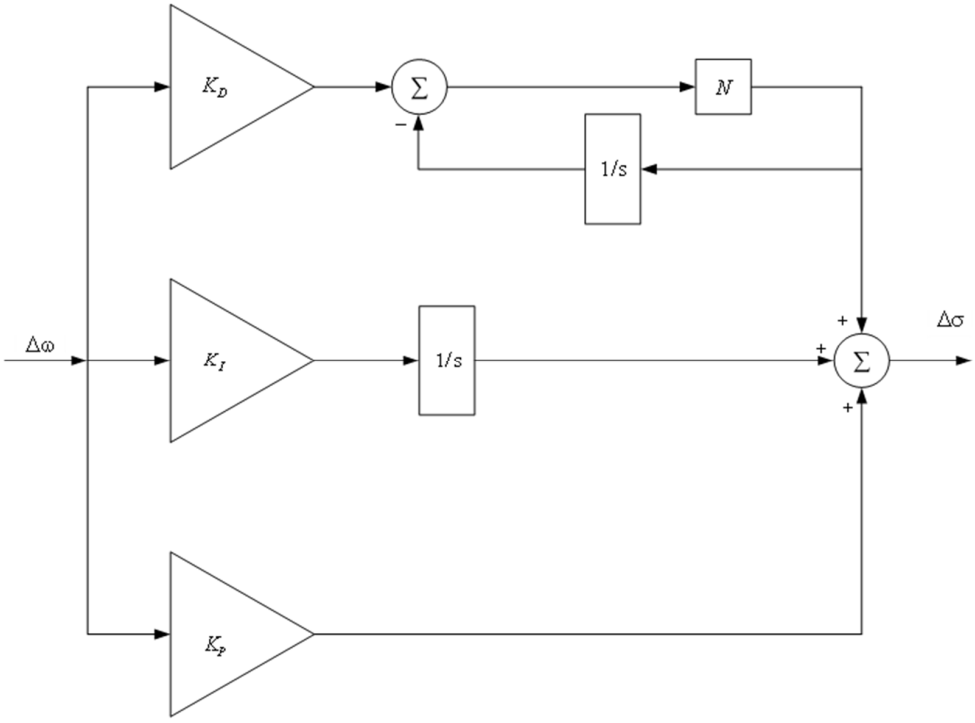


Figure 3. Block diagram of the PIDF controller.

A block diagram of the TCSC PIDF controller with a speed deviation in the SMIB system is shown in Figure 4.

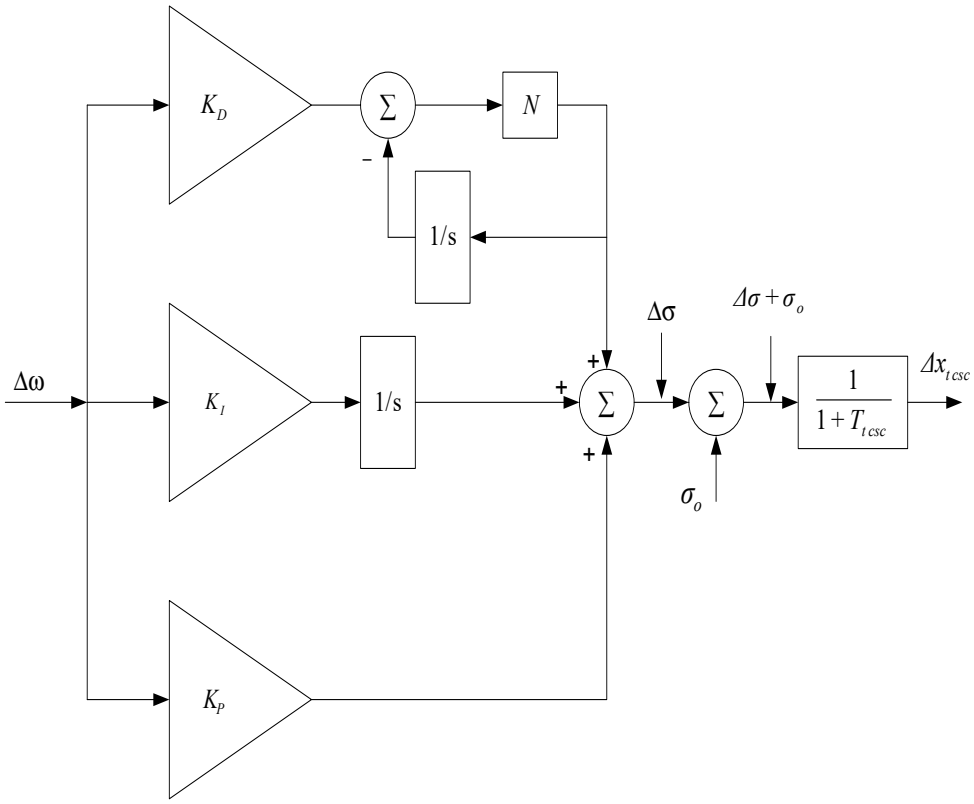


Figure 4. Block diagram of the TCSC PIDF controller.

The values of Equation (26) are placed in Equation (35), and Equations (36)–(42) are the extended Phillips–Heffron model of the single-machine infinite-bus power system installed with a PIDF controller and TCSC stabiliser.

$$\Delta\dot{\delta} = \omega_o \Delta\omega \tag{36}$$

$$\Delta\dot{\omega} = [-K_1\Delta\delta - \mathrm{D}\Delta\omega - K_2\Delta\acute{E}_q - K_p\Delta x_{tscc}]/M \tag{37}$$

$$\Delta\dot{\acute{E}}_q = \frac{1}{\acute{T}_{do}}(-K_4\Delta\delta - K_3\Delta\acute{E}_q - K_q\Delta x_{tscc} + \Delta\acute{E}_{fd}) \tag{38}$$

$$\Delta\dot{\acute{E}}_{fd} = -\frac{\Delta\acute{E}_{fd}}{T_A} - \frac{K_A}{T_A}(K_5\Delta\delta + K_6\Delta\acute{E}_q + K_v\Delta x_{tscc}) \tag{39}$$

$$\Delta\dot{\sigma} = \Delta f \tag{40}$$

$$\Delta\dot{f} = G\Delta\delta + H\Delta\omega + I\Delta\acute{E}_q + J\Delta\acute{E}_{fd} - L\Delta\sigma - N\,\Delta f + K\Delta x_{tcsc} \tag{41}$$

$$\Delta\dot{x}_{tcsc} = \frac{1}{T_{tcsc}}\Delta f - \frac{1}{T_{tcsc}}\Delta x_{tcsc} \tag{42}$$

where G, H, I, J, K, L, and N are constants.

$$\dot{X} = A_{PIDF}.\mathrm{X} + B_{PIDF}.\mathrm{U} \tag{43}$$

$$\dot{X} = [\Delta\dot{\delta}\ \ \Delta\dot{\omega}\ \ \Delta\dot{\acute{E}}_q\ \ \Delta\dot{\acute{E}}_{fd}\ \ \Delta\dot{\sigma}.\ \ \Delta\dot{f}\ \ \Delta\dot{x}_{tcsc}] \tag{44}$$

$$\mathrm{X} = [\Delta\delta\ \ \Delta\omega\ \ \Delta\acute{E}_q\ \ \Delta\acute{E}_{fd}\ \ \Delta\sigma\ \ \Delta f\ \ \Delta x_{tcsc}] \tag{45}$$

$$A_{PIDF} = \begin{bmatrix} 0 & \omega_o & 0 & 0 & 0 & 0 & 0 \\ -\frac{K_1}{M} & -\frac{D}{M} & -\frac{K_2}{M} & 0 & 0 & 0 & -\frac{K_p}{M} \\ -\frac{K_4}{T'_{do}} & 0 & -\frac{K_3}{T'_{do}} & \frac{1}{T'_{do}} & 0 & 0 & -\frac{K_q}{T'_{do}} \\ -\frac{K_A K_5}{T_A} & 0 & -\frac{K_A K_6}{T_A} & -\frac{1}{T_A} & 0 & 0 & -\frac{K_A K_v}{T_A} \\ 0 & 0 & 0 & 0 & 0 & 1 & 0 \\ G & H & I & J & -L & -N & K \\ 0 & 0 & 0 & 0 & 0 & \frac{1}{T_{t\,\mathrm{csc}}} & -\frac{1}{T_{t\,\mathrm{csc}}} \end{bmatrix} \quad (46)$$

$$B_{PIDF} = \begin{bmatrix} 0 \\ \frac{1}{M} \\ 0 \\ 0 \\ 0 \\ 0 \\ 0 \end{bmatrix} \quad (47)$$

$$U = [\Delta T_m] \quad (48)$$

2.3. Objective Function

The MO function is a mathematical illustration that indicates that more than one goal needs to be accomplished through optimisation. In general, the increase in damping ratio is correlated with the improvement of overshoot in oscillations [41]. However, the damping factor improves the settling time of the electromechanical modes of oscillations. Eigenvalue sectors will move simultaneously towards the real axis and away from the imaginary axis of the real–imaginary plane with the use of MO functions based on both $\zeta_{\min}$ and $\sigma_{\max}$ [23], where $\zeta_{\min}$ is the minimum value of an eigenvalue among the system eigenvalues, and $\sigma_{\max}$ is the maximum value of the real part of an eigenvalue among the system eigenvalues.

Figure 5 displays the association among the eigenvalue sectors, pre-optimised MO, and post-optimised MO on the real–imaginary plane. This post-implementation of the MO eigenvalue scattering pattern somewhat resembles a wedge shape, tapering from the left to the right of the complex s-plane.

In this work, an MO function is proposed, which gives equal weight to the damping factor, damping ratio, and eigenvalues. This method formulates the MO function by using the algebraic sum of the damping factor and the damping ratio of the d-shaped region of the s-plane.

$$\text{Objective function} = a_1.\zeta_{\min} + a_2.\ \frac{\sigma_{max}}{\sigma_{min}} + a_3.\ \frac{1}{1 + |\omega_{max}|} \quad (49)$$

where $\zeta_{\min}$ expresses the minimum damping ratio; σ_{max} and σ_{min} are the maximum and minimum damping factors, respectively; and $|\omega_{max}|$ refers to the absolute value of the maximum imaginary part of system eigenvalues; a_1 = 0.1, a_2 = 0.4, and a_3 = 0.5. Parameters a_1, a_2, and a_3 are determined based on an initial test that determines whether the selected values are suitable for indicating the stability of the power system.

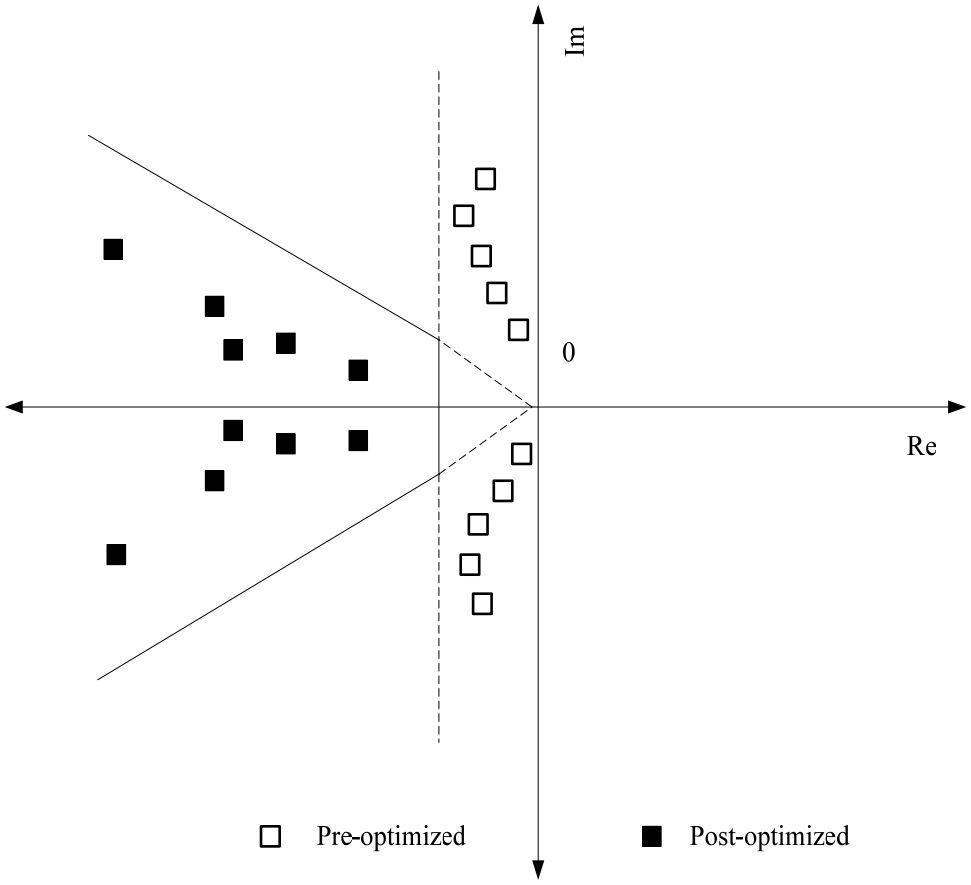


Figure 5. Correlation of eigenvalue sectors (pre- and post-optimised MO).

3. Proposed Algorithm

The term 'optimisation' describes the process of selecting from among all feasible values the parameters that will maximise or decrease the output of a particular system. Optimisation issues occur in all academic disciplines. Over the past two decades, interest in stochastic optimisation approaches has increased due to the shortcomings of traditional optimisation techniques, local optima stagnation, and the requirement to derive the search space. These optimisation paradigms simply alter the system's inputs and track its outputs to maximise or minimise its outputs, whereas stochastic algorithms have the advantages of high flexibility and random optimisation of optimisation problems.

The limitation of evolutionary-based algorithms, such as EP, is premature convergence as a result of the local minimum stagnation problem. EP functions more effectively during the exploitation phase than during the exploration phase. The EP optimisation technique has a low rate of convergence and cannot handle multimodal issues [22]. The sine cosine algorithm (SCA) is a population-based algorithm that operates in two phases—exploration and exploitation—and starts with a collection of random solutions. The SCA optimisation technique yields superior results when used to explore and exploit the eigenvalue analysis' maxima and minima. However, the SCA method converges the solution within a slightly higher number of iterations. In sum, the EP algorithm is fast and inaccurate, while SCA is an accurate approach, although it takes more time to complete. The combination of EP and SCA will give accurate results within a shorter time.

3.1. Evolutionary Programming Sine Cosine Algorithm

The evolutionary programming sine cosine algorithm (EPSCA) is a hybrid technique that combines the features of the EP algorithm and SCA. The concept of mutation was implemented by modifying the existing features of the SCA technique. This concept has

four more steps in the SCA algorithm. In the first step, a random number v_5 ranging from zero to one is updated. In the second step, an updated and best solution given by SCA is mutated based on two techniques: Levy flight or random number. In the third step, the mutated candidate's solutions and clone solutions are combined. The algorithm then updates each candidate solution. In the last step, half of the candidates are selected based on optimal solutions, and the best optimal solution is chosen. The varying positions for both phases are represented by the equation below:

$$Y_{i,j}^{u+1} = Y_{i,u} + v_1^u \times \sin v_{2,j} \times \left| v_{3,j} R_{d,j}^u - Y_{i,j}^u \right| \tag{50}$$

$$Y_{i,j}^{u+1} = Y_{j,u} + v_1^u \times \cos v_{2,j} \times \left| v_{3,j} R_{d,j}^u - Y_{i,j}^u \right| \tag{51}$$

Equations (50) and (51) are combined to be applied as follows:

$$Y_{i,j}^{u+1} = \begin{cases} Y_{i,u} + v_1^u \times \sin v_{2,j} \times \left| v_{3,j} R_{d,j}^u - Y_{i,j}^u \right|, \ v_{4,j} < 0.5 \\ X_{j,u} + v_1^u \times \cos v_{2,j} \times \left| v_{3,j} R_{d,j}^u - Y_{i,j}^u \right|, \ v_{4,j} \geq 0.5 \end{cases} \tag{52}$$

where u denotes the current iteration; $R_{d,j}^u$ is the location of the destination in the jth dimension; $Y_{i,u}$ is the current solution at the uth iteration; v_1^u, $v_{2,j}$, and $v_{3,j}$ are random values; $v_{4,j}$ is a random number between 0 and 1; and $| \ |$ is an absolute value.

SCA has four main parameters—v_1^u, $v_{2,j}$, $v_{3,j}$, and $v_{4,j}$—as shown by the aforementioned equations. The parameter v_1 determines the subsequent location regions (or movement direction), which may be inside or outside the region between the solution and the destination. The parameter $v_{2,j}$ specifies how far the movement should extend in either direction from the target. The value of the parameter v_3 determines random weights for the destination to stochastically emphasise or deemphasise the role of the destination in determining the distance. The parameter r_4 then alternates equally between the sine and cosine parts of Equation (52). Equation (53), which is written as follows, changes the sine and cosine ranges to find a favourable region in a given domain and converge it to the universal optima, thereby allowing the SCA algorithm to maintain balance during exploitation and exploration:

$$v_1^u = \mathrm{b} - \mathrm{u} \ \frac{b}{U} \tag{53}$$

where U is the maximum number of iterations, b is a constant value, and u represents the current iteration. Levy flight is a generalised Brownian motion random walk method, and the duration of its steps for distance travel follows a non-Gaussian random distribution known as the Levy stable distribution. The Levy distribution can be described mathematically as follows:

$$L_f(\mathrm{z}, \mathrm{q}, \mathrm{r}) = \begin{cases} \sqrt{\frac{q}{2\pi}} \exp\left(\frac{-q}{2(z-r)}\right) \frac{1}{(z-r)^{\frac{3}{2}}}, 0 < r < \infty \text{ and } 0 < z < \infty \\ 0, z \leq 0 \end{cases} \tag{54}$$

where the scale parameter q controls the distribution scale, and the location parameter r controls the location. The offspring's standard deviation is expressed as follows:

$$\zeta_k = \text{Ƙ}. \frac{G(y_l)}{G_{max}} (p_k^{max} - p_k^{min}), \tag{55}$$

where each parent y_l produces one offspring y_{l+n}. Each optimised parameter p_k is perturbed by a Gaussian random variable $N(0, \zeta_1^2)$. y_l is the trial solution of fitness equation $G(y_l)$, and Ƙ is a scaling factor. G_{max} represents the maximum value of the fitness function. The offspring y_{l+n} can be defined as follows:

$$y_{l+n} = y_l + \left\{ N\left(0, \zeta_1^2\right), \ldots, N\left(0, \zeta_m^2\right) \right\}, \tag{56}$$

combine (combination) (2n candidates), where $l = 1, \ldots, n$.

All individuals' objective functions are determined. If $G_{max} < G_{best}$, then the (combination) best solution and best results from the mutation process (2n candidates) are combined, and all individuals from the population y_l are joined with all individuals from its offspring, y_{l+n}. Subsequently, these individuals are arranged in decreasing order, using their weight as their objective function. Later, the first n individuals with greater weights are chosen together with their objective functions for the next generation. The search process is stopped when the difference between G_{max} and G_{min} is zero. Upon failure to stop the search process, the algorithm will start again from Equation (52). If $G_{max} > G_{best}$, then the best solution is . $G_{max} = G_{best}$ is updated. Subsequently, the algorithm will start again from the combination point. Figure 6 shows the flowchart of the EPSCA.

The SCA allows exploration and exploitation in a search space for the first and second iterations, respectively. This ability distinguishes it from other algorithms. The main benefit of using SCA optimisation is that it produces better results when exploring and exploiting the eigenvalue analysis space to find maxima or minima. SCA has some limitations in the search exploitation approach for fast convergence. SCA optimisation takes time to achieve quality solutions and has difficulty deriving consistent solutions for a system that requires a large amount of parameter optimisation. The SCA solution performance may be improved by its convergence rate and solution consistency. The improved version of SCA is hybrid EPSCA, which provides solution performance by its convergence rate and solution consistency and may be used to optimise the damping controller in an SMIB and multimachine systems.

3.2. Sine Cosine Algorithm

In recent years, the SCA, a new metaheuristic method, has been proposed. SCA repeats certain random steps by selecting sine or cosine functions to discover the global optimum. Strong randomness patterns have been observed in SCA's search patterns. Mirjalili created SCA, a stochastic population-based optimisation metaheuristic technique. A system's parameters can be optimised by following a method or mathematical procedure to find the optimum values possible in the search space. SCA is a population-based algorithm that operates in two phases—exploration and exploitation—and starts with a set of random solutions. As part of the exploration phase, the algorithm generates a set of results that include unusually high-rate random outcomes, allowing it to identify potential places in the search space. The algorithm primarily highlights the incremental variations in random solutions during the exploitation phase [42]. The shifting positions for both phases are represented by the equation below.

$$X_{i,j}^{t+1} = X_{i,t} + r_1^t \times \sin r_{2,j} \times \left| r_{3,j} Q_{d,j}^t - X_{i,j}^t \right| \tag{57}$$

$$X_{i,j}^{t+1} = X_{j,t} + r_1^t \times \cos r_{2,j} \times \left| r_{3,j} Q_{d,j}^t - X_{i,j}^t \right| \tag{58}$$

Equations (57) and (58) are combined to be applied as follows.

$$X_{i,j}^{t+1} = \begin{cases} X_{i,t} + r_1^t \times \sin r_{2,j} \times \left| r_{3,j} Q_{d,j}^t - X_{i,j}^t \right|, & r_{4,j} < 0.5 \\ X_{j,t} + r_1^t \times \cos r_{2,j} \times \left| r_{3,j} Q_{d,j}^t - X_{i,j}^t \right|, & r_{4,j} \geq 0.5 \end{cases} \tag{59}$$

where t is the current iteration; $Q_{d,j}^t$ is the target location in the jth dimension; $X_{i,t}$ is the current solution at the tth iteration; and the random variables r_1^t, $r_{2,j}$, and $r_{3,j}$ are all present. $r_{4,j}$ is a random number between 0 and 1, and || displays an absolute value.

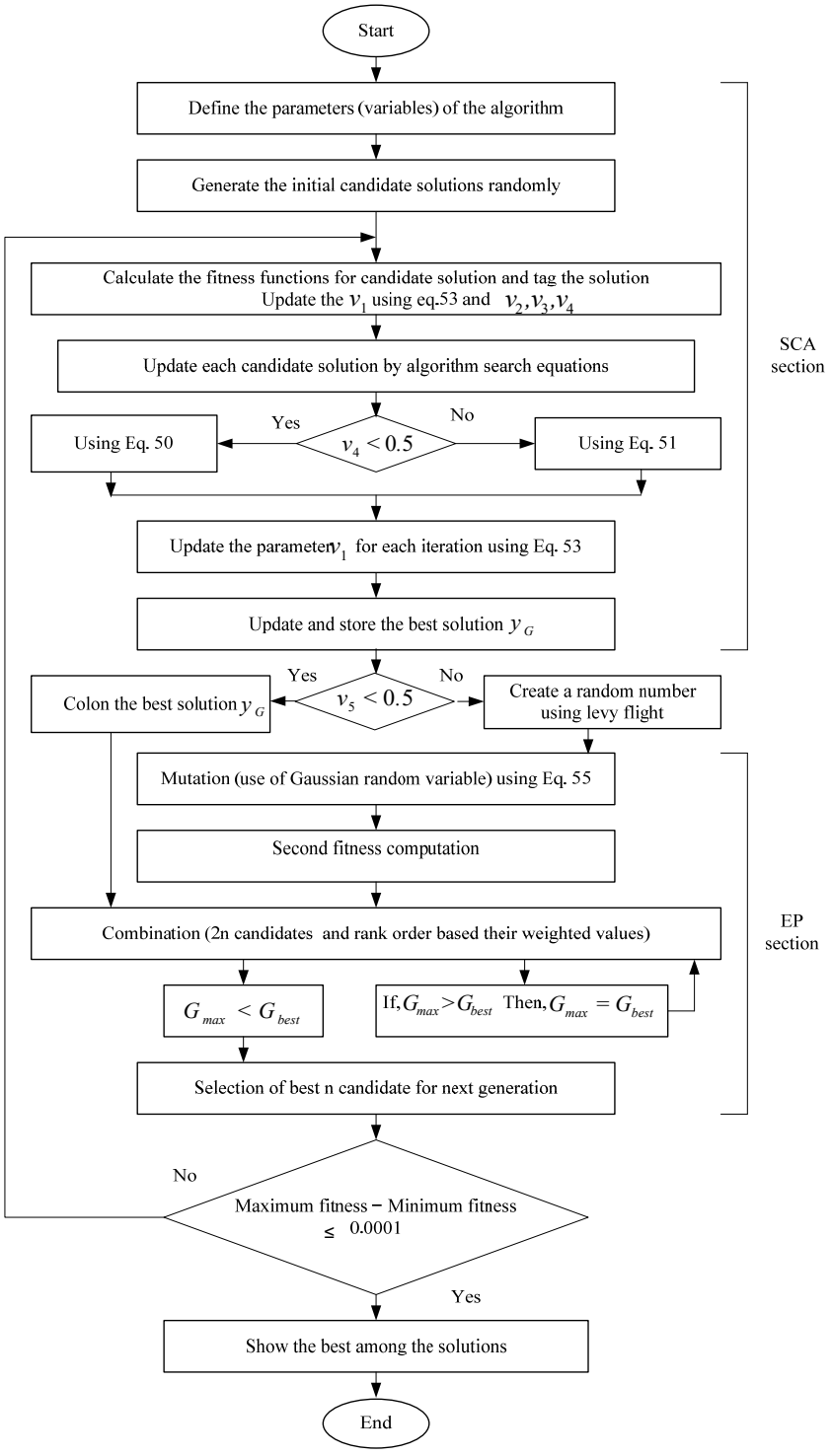


Figure 6. EPSCA flowchart.

SCA has four main parameters—r_1^t, $r_{2,j}$, $r_{3,j}$, and $r_{4,j}$—as shown by the aforementioned equations. The parameter r_1 determines the subsequent location regions (or movement direction), which may be inside or outside the region between the solution and the destination. The parameter $r_{2,j}$ specifies how far the movement should extend in either direction from the target. The value of the parameter r_3 determines random weights for the destination to stochastically emphasise or deemphasise the role of the destination in determining the distance. The parameter r_4 then alternates equally between the sine and cosine parts of

Equation (59). The SCA algorithm creates a balance between exploitation and exploration by adjusting the sine and cosine ranges using Equation (60), which is written as follows:

$$r_1^t = \mathrm{a} - \mathrm{t}\frac{a}{T} \tag{60}$$

where T is the maximum number of iterations, a is a constant number, and t is the current iteration. Figure 7 provides a two-dimensional illustration of the effects of sine and cosine on Equations (57) and (58), which can be expanded to higher dimensions. The patterns of these equations allow a solution to reposition and guarantee exploitation of a region between two results, and they specify a domain between two results in a specified search domain. To regulate the exploration in a specific search domain, the optimisation approach should look outside the area that contains subsequent destinations. Figure 8 illustrates the cosine sine functions obtained when changing the amplitude range. Whether a location is within or outside is determined by the random integer $r_{2,j}$, whose range is (0, 2) [42]. Figure 9 depicts the SCA flowchart.

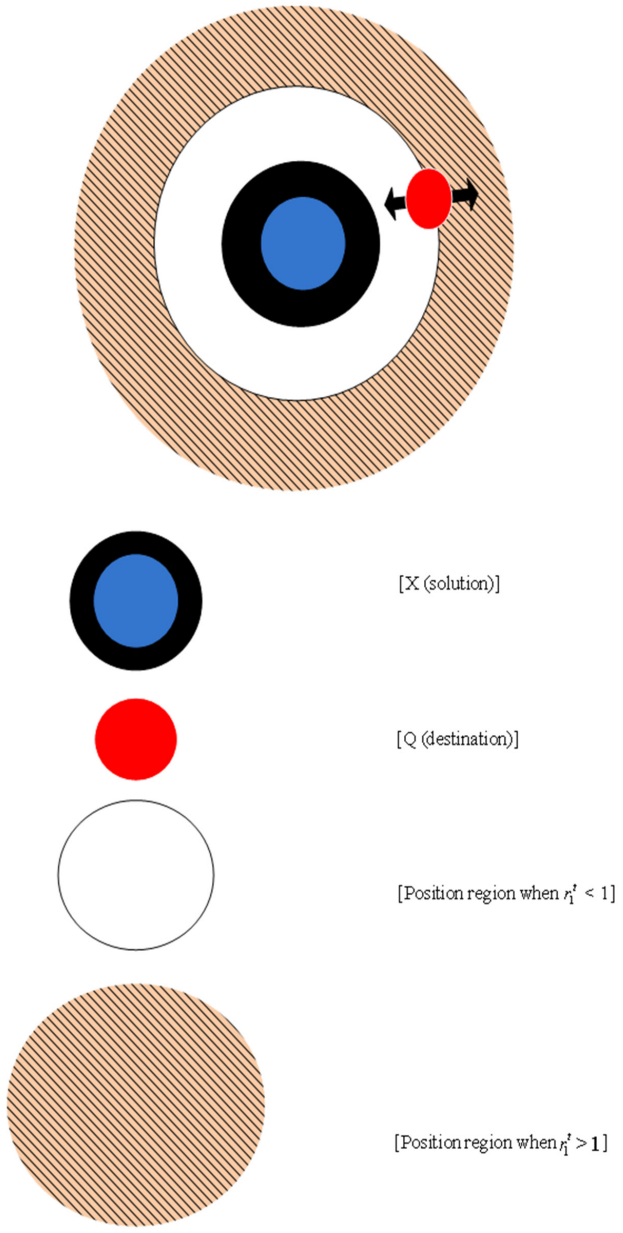


Figure 7. Sine and cosine effects on the forthcoming locality in Equations (57) and (58).

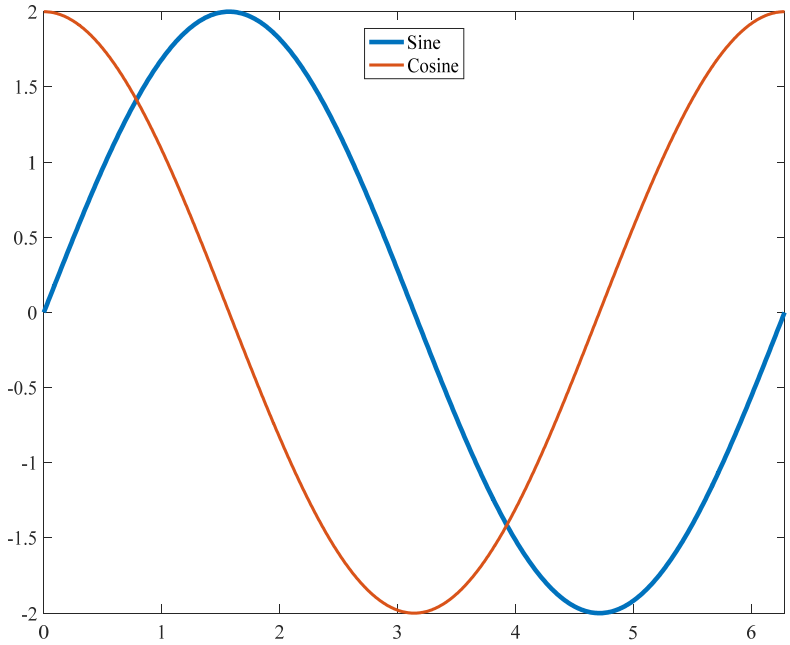


Figure 8. Amplitude scale of $(-2, 2)$ and a period range of $(0, 2\pi)$ for sine and cosine.

3.3. Moth Flame Optimisation Algorithm

Moths are insects similar to butterflies, and their most remarkable aspect is their unique night-time navigational system; they have evolved to use moonlight to fly at night and use transverse orientation as a navigational tool. By maintaining a steady angle with respect to the moon, this mechanism enables the moth to fly, making it an efficient way to cover large distances in a straight line. A conceptual model of transverse orientation is shown in Figure 10. This system ensures straight-line flight because the moon is far from the moth. Humans can use the same navigating technique. Consider a scenario in which the moon is on the south side of the sky and a person is heading east. He or she could walk in a straight line towards the east if he/she keeps the moon on his/her left side while doing so [43].

As seen in Figure 11, a moth flies spiralling around a light rather than in a straight line because only when the light source is very far away does the transverse orientation method work effectively (moonlight). Moths try to maintain the same angle as the light source in the case of artificial light. Following that idea, moths are seen flying in spiral patterns around lights.

To develop the moth flame optimisation (MFO) algorithm, mathematical models of moth flight behaviour were used. MFO is a metaheuristic algorithm that defines parameters firstly, creates moths at random, determines each moth's position, and tags the optimal response in relation to the light source (flame). To achieve better locations in relation to the light source, the moths' future positions are modified based on the spiral path function. The requirements are satisfied (after obtaining the best solution) when this process, which involves updating the next positions and tagging the best solutions with respect to the flame, is completed [43]. Three main steps make up MFO: the creation of the initial moth population, the updating of the moth positions, and the updating of the flame count. Creating the initial population of moths in the first stage assumes that each moth can move in multiple dimensions. The moths' set (M) matrix is as follows:

$$M = \begin{bmatrix} M_{11} & M_{12} & \cdots & M_{1d} \\ M_{21} & M_{22} & \cdots & M_{2d} \\ \vdots & \vdots & \vdots & \vdots \\ M_{n1} & M_{n2} & \cdots & M_{nd} \end{bmatrix} \tag{61}$$

where n is the quantity of moths, and d is the spatial dimension. The fitness values OM are kept in an array for all moths.

$$\mathrm{OM} = \begin{bmatrix} OM_1 \\ OM_2 \\ \vdots \\ OM_n \end{bmatrix} \tag{62}$$

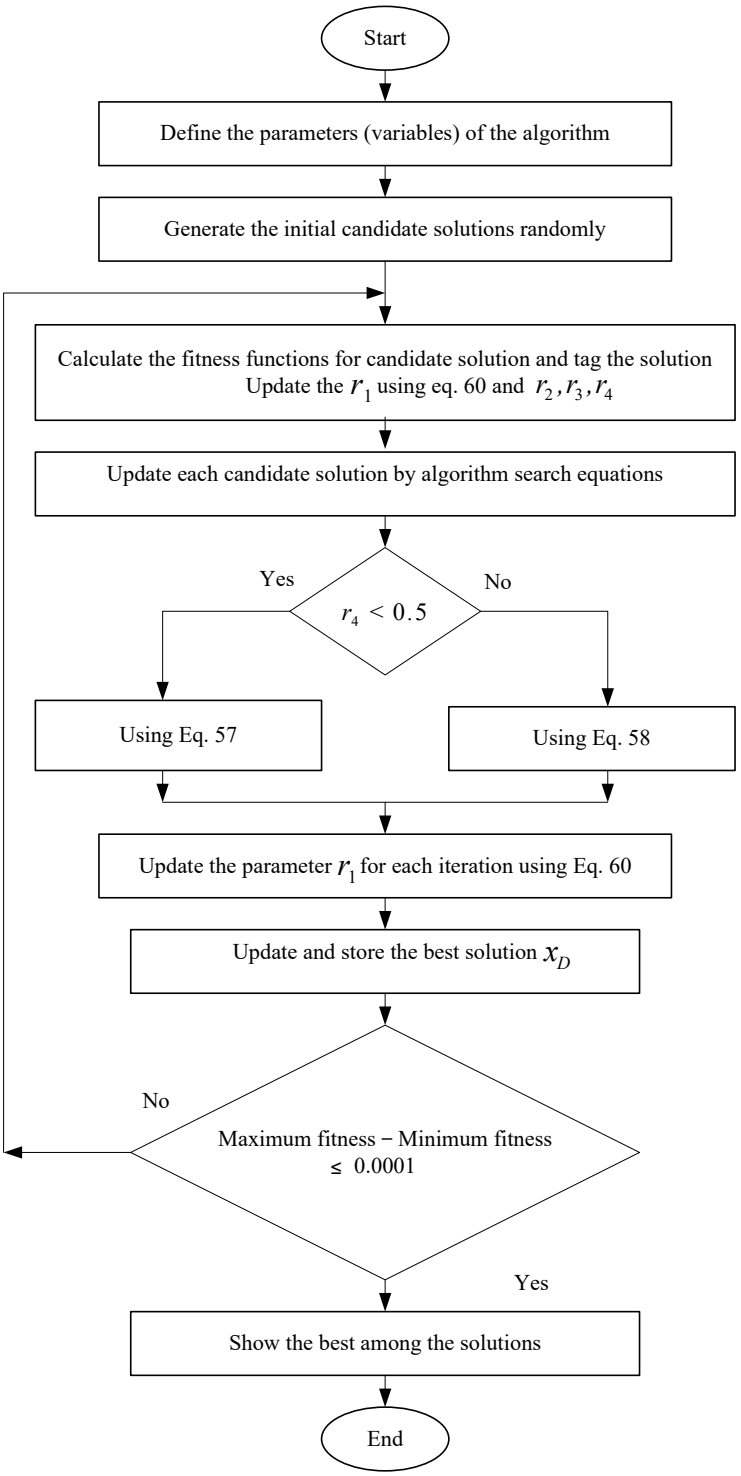


Figure 9. SCA flowchart.

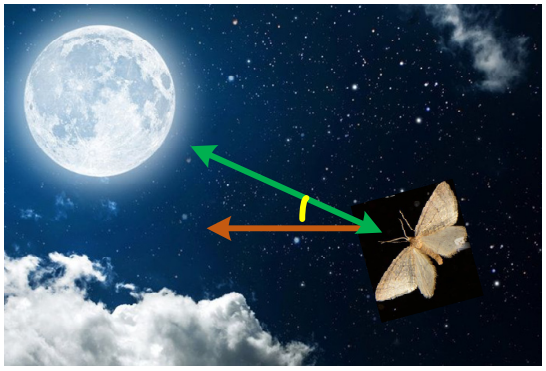


Figure 10. Transverse orientation of a moth.

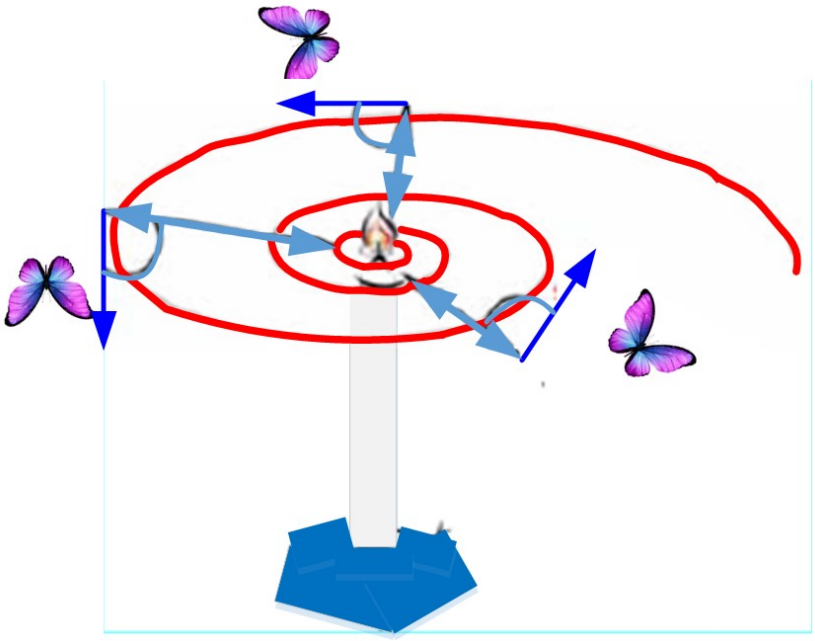


Figure 11. A moth's spiral flight route around a source of light.

The following describes the set of flames (F) in d-dimensional space as a matrix:

$$F = \begin{bmatrix} F_{11} & F_{12} & \cdots & F_{1d} \\ F_{21} & F_{22} & \cdots & F_{2d} \\ \vdots & \vdots & \vdots & \vdots \\ F_{n1} & F_{n2} & \cdots & F_{nd} \end{bmatrix} \tag{63}$$

The fitness values of all flames are kept in an array.

$$\mathrm{OF} = \begin{bmatrix} OF_1 \\ OF_2 \\ \vdots \\ OF_n \end{bmatrix} \tag{64}$$

Secondly, three functions are used to update the moth positions to converge to the global optimum.

$$MFO = (I, P, T) \tag{65}$$

where I denotes the moth's initial location within the search area, P is its motion within the area, and T is its destination. Function I can be represented by the following equation:

$$M\ (i, j) = (ub(i) - lb(j))\ *\text{rand}\ () + lb(i) \tag{66}$$

where the variable's upper and lower bounds are indicated by *ub* and *lb*, respectively. The MFO algorithm's logarithmic spiral equation ensures that the moth near the flame will be explored and used in the search space, as follows:

$$S(M_i, F_j) = D_i.e^{bt}.cos(2\pi t) + F_j \tag{67}$$

where b is the spiral shape, t is a value between 1 and 1, and D_i is the distance between the ith moth and the jth flame. The following is the formula for D_i:

$$D_i = |F_j - M_i| \tag{68}$$

Figure 12 shows the logarithmic spiral, the area around the flame and the position of the moth considering the different value of t. The spiral flight path of moths is modelled in Equation (67). This equation illustrates how a moth's future position in relation to a flame is determined. The spiral equation's t parameter specifies how close the moth should be to the flame in its subsequent positions ($t = -1$ represents its closest position and t = 1 represents its farthest). As a result, a hypercircle that surrounds the flame in all directions can be visualised, and the moth would then be in this area. The fundamental element of the suggested strategy is spiral movement because it controls how the moths update their positions near flames. A moth can fly 'around' a flame according to the spiral equation, rather than necessarily in the area between them. As a result, it is possible to ensure that the search space will be explored and used [43].

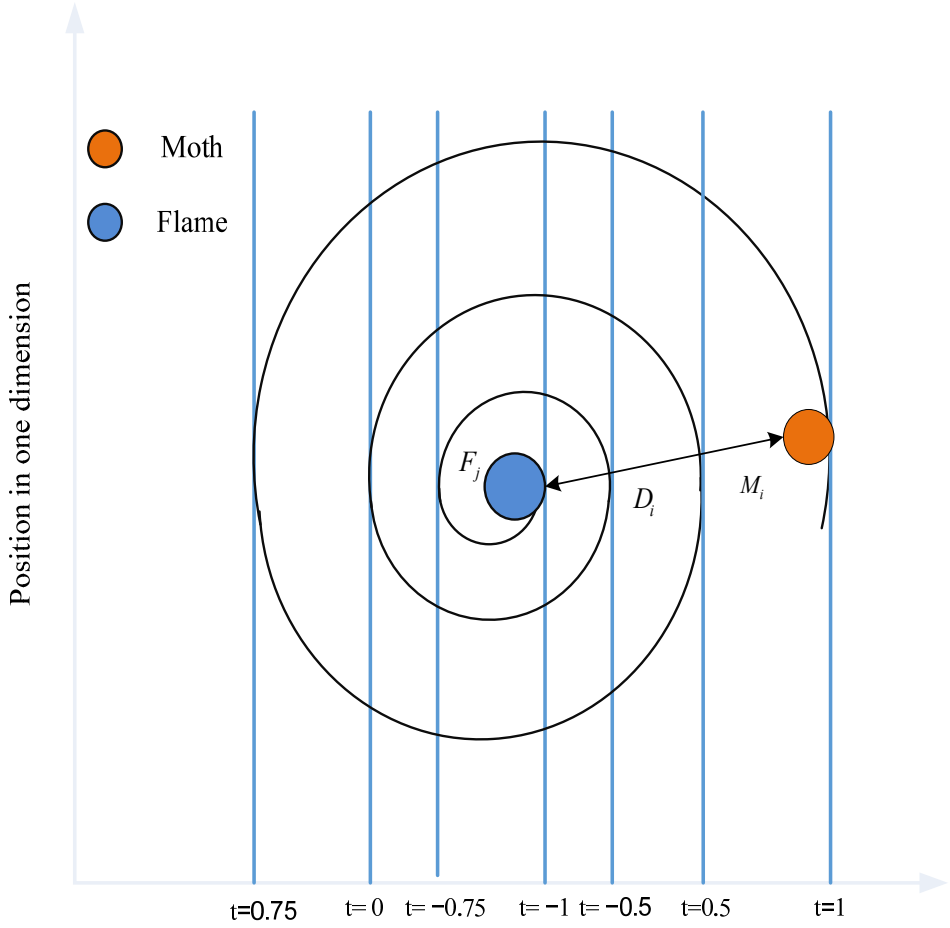


Figure 12. Space surrounding a flame, a logarithmic spiral, and the position in relation to t.

While it simply requires the moths to move in the direction of the flame, the position update in Equation (67) results in the MFO algorithm becoming rapidly stuck in the local optima. To avoid this situation, each moth is required to update its location by utilising just one of the flames in Equation (67). The flames are sorted according to their fitness levels after the list of flames is updated after each iteration. In relation to their associated flames, the moths then update their positions. The first moth always adjusts its position in relation to the best flame in the list, whereas the last moth does so in relation to the poorest flame. Another issue with this approach is that the exploitation process can suffer from the moths' positions being updated in relation to n different flames (locations) in the search space. The quantity of flames is adaptively reduced during the course of iterations, as follows, to address this concern:

$$\text{Flame no.} = \text{round}\ (N - l\ \frac{N-l}{T}) \tag{69}$$

where T is the maximum number of iterations, N is the maximum number of flames, and l is the current iteration number. As previously mentioned, the P function is executed until the T function returns true. Once the P function is terminated, the best moth is returned as the best approximation of the optimum [43]. The MFO algorithm's flowchart is depicted in Figure 13.

3.4. Evolutionary Programming Algorithm

The EP algorithm is a natural process-based heuristic method designed to find the best answer in the search space (i.e., biological evolution and population, both for random and selection). The six main steps of this algorithm are as follows: Initialisation involves producing random results; the mutation process uses a Gaussian random variable; statistics are obtained by computing the high, low, and average values of a fitness function; the best results and combinations are updated; the highest value of the fitness function is chosen for the next iteration; and the programme is shut down once the predetermined criteria have been met. The offspring's standard deviation is expressed as follows:

$$\varsigma_k = \beta . \frac{J(x_l)}{J_{max}} (p_k^{max} - p_k^{min}), \tag{70}$$

where each x_l parent creates one x_{l+n} offspring. An $N\ (0, \sigma_1^2)$ Gaussian random variable perturbs each optimised parameter p_k. The trial solution to the fitness equation $J(x_l)$ is x_l, and the scaling factor J_{max} which stands for the fitness function's maximum value. The offspring x_{l+n} can be defined as follows:

$$x_{l+n} = x_l + \left\{ N\ (0, \sigma_1^2\ ),\ \ldots,\ N\ (0, \sigma_m^2) \right\}, \tag{71}$$

where $l = 1, \ldots, n$. All individuals' objective functions are determined; if $J_{max} < J_{best}$, then to create 2n candidates (combination), all individuals from the population x_l are joined with all individuals from its offspring, x_{l+n}. Subsequently, using their weight as their objective function, these individuals are ordered in decreasing order. Later, the first n individuals with greater weights are chosen together with their objective functions for the next generation. Afterwards, the search process is stopped once the difference between J_{max} and J_{min} is zero. Upon failure to stop the search process, the algorithm will start again from Equation (70). If $J_{max} > J_{best}$, then the best solution x_{best} is updated. $J_{max} = J_{best}$. Subsequently, the algorithm will start again from the combination point [22,24,44]. The EP algorithm's flowchart is depicted in Figure 14.

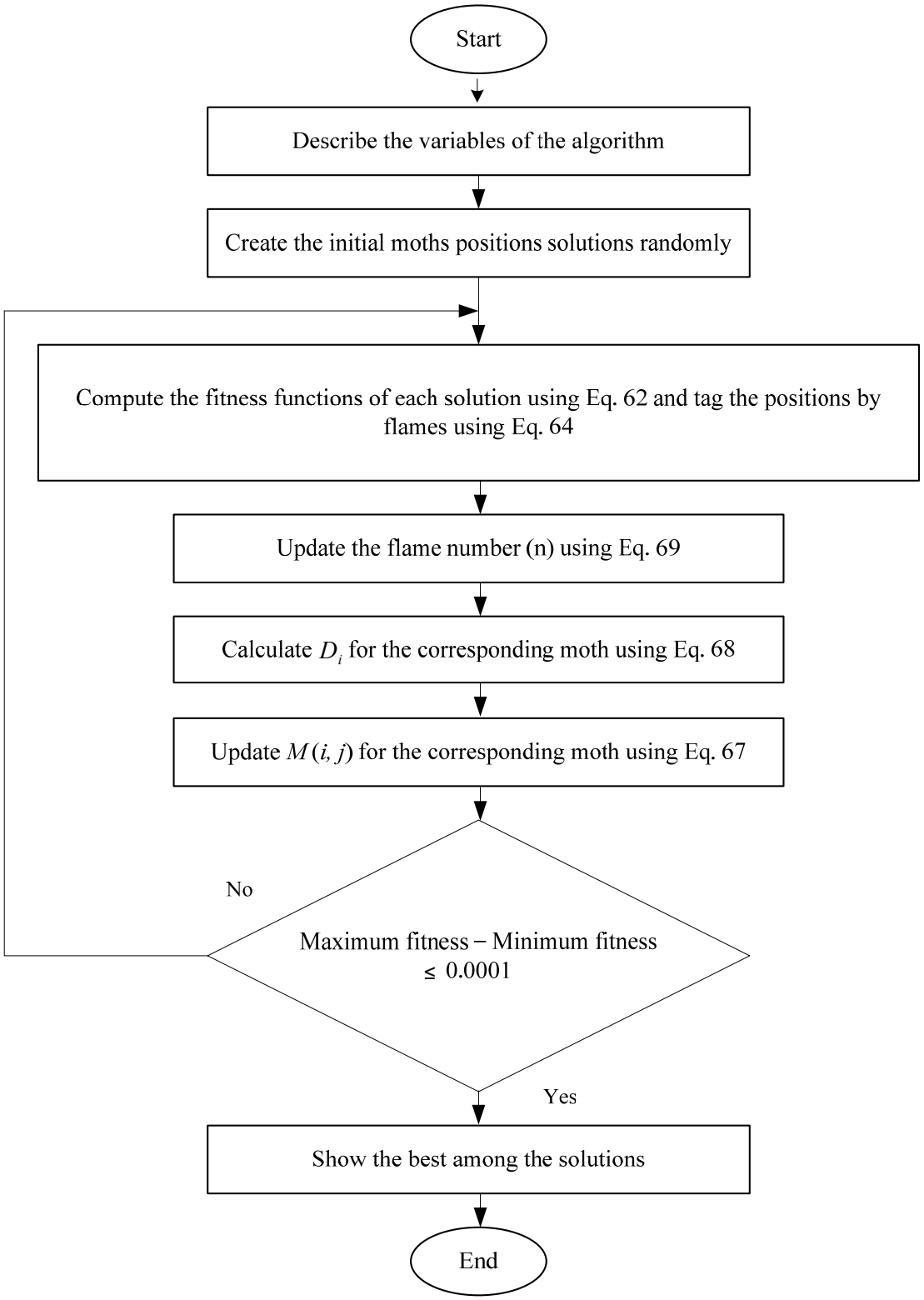


Figure 13. MFO flowchart.

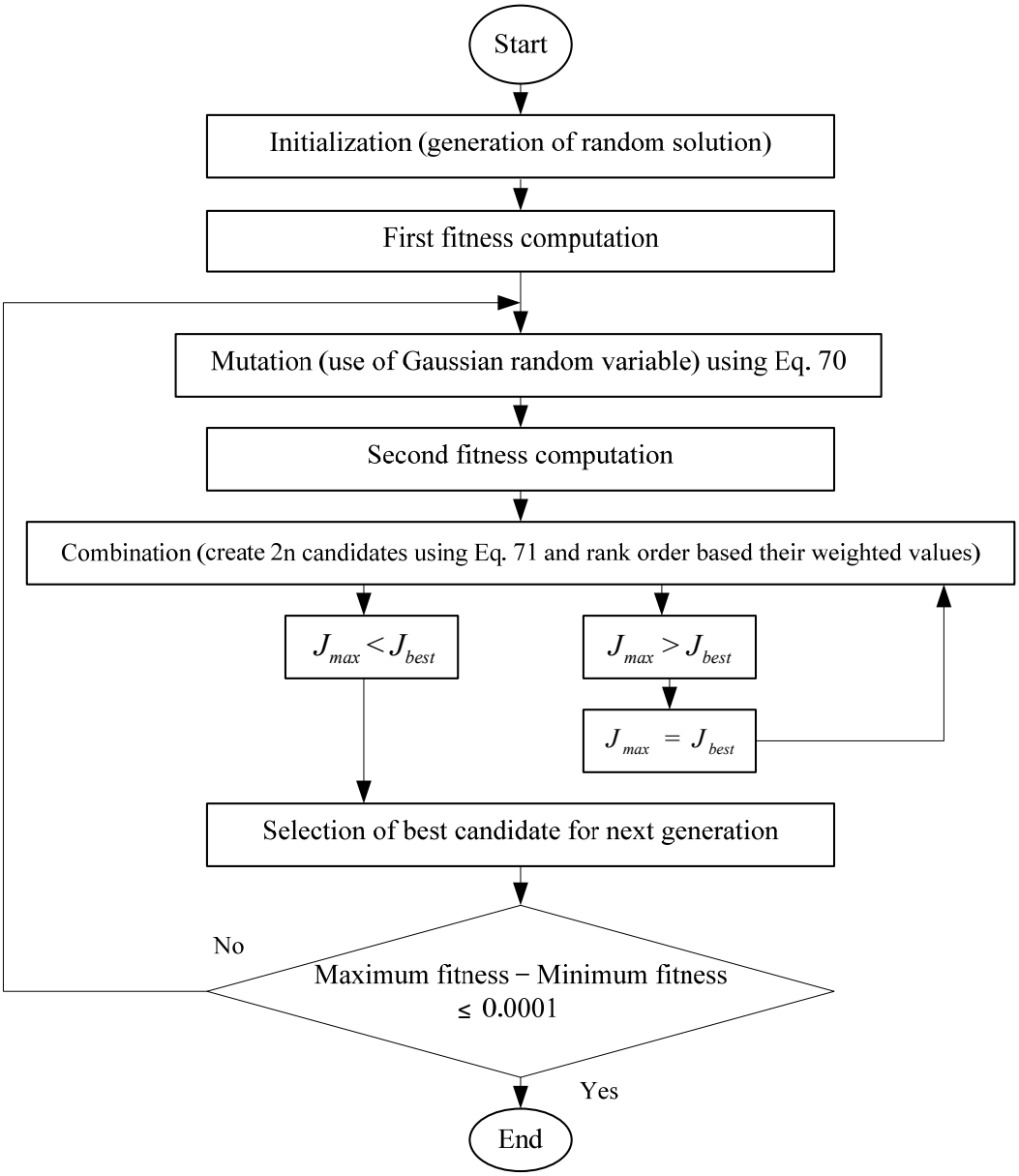


Figure 14. EP flowchart.

4. Results

The results and discussion of the MO function strategy for improving oscillation stability in the SMIB system by utilising a variety of optimisation strategies are presented in this part. The four scenarios with various loading conditions are given in Table 1. The TCSC PIDF (SMIB-TCSC-PIDF) was used in MATLAB to conduct all cases.

Table 1. Scenarios involving the loading conditions.

Scenarios	Loading Scenarios (P, Q)	
	Dynamic Load (P)	Reactive Load (Q)
Scenario A-1	P = 0.500 (p.u)	Q = 0.3155 (p.u)
Scenario A-2	P = 0.475 (p.u)	Q = 0.3172 (p.u)
Scenario A-3	P = 0.400 (p.u)	Q = 0.3219 (p.u)
Scenario A-4	P = 0.300 (p.u)	Q = 0.3269 (p.u)

The following four strategies are discussed:

1. TCSC-PIDF controller in an SMIB system that was optimised using EPSCA (PIDF-EPSCA).
2. TCSC-PIDF controller in an SMIB system that was optimised using SCA (PIDF-SCA).
3. TCSC-PIDF controller in an SMIB system that was optimised using MFO (PIDF-MFO).
4. TCSC-PIDF controller in a SMIB system that was optimised using EP (PIDF-EP).

Table 2 shows the parameters of SMIB and TCSC.

Table 2. SMIB and TCSC parameter values.

Modules	Parameters List
Generator	H = 4, x_d = 1.0, R_a = 0.005, x_q = 0.78, x_Q = 0.73, x_D = 1.11, $T_{d0'}$ = 6, x_{ad} = 1, x_{aq} = 0.6.r_D = 0.002, M = 7, r_Q = 0.04.
Transmission Line	R_e = 0, x_t = 0.15.
Exciter and TCSC	K_A = 10, T_A = 0.02, V_{bo} = 1.0, V_{to} = 1.05, x_L = 0.054, x_{tcsc} = 0.90837, V_b = 1.

Figure 15 shows the angle deviation response for Scenario A-1. When compared with other scenarios, PIDF-EPSCA exhibited the smoothest response and minimum swing for angle deviation response. The system was damped 1.35 s after the simulation began. PIDF-SCA was in second place, followed by PIDF-MFO and PIDF-EP. The PIDF-EP system was at the last position, taking a longer time to dampen the oscillation out of all four techniques. Except for PIDF-EPSCA, the damping time of the other techniques was longer than 2 s.

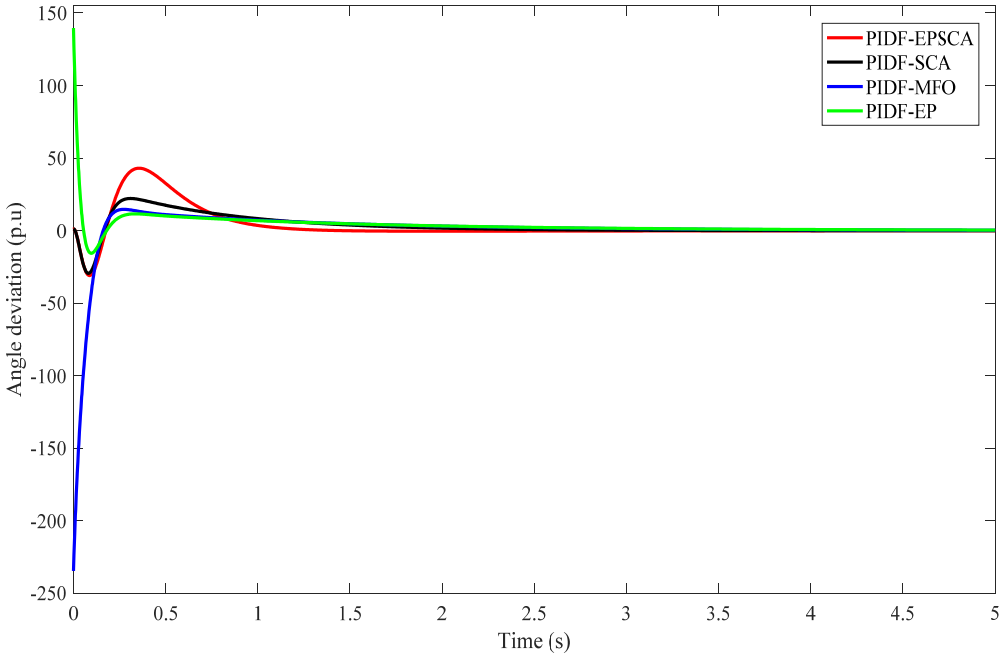


Figure 15. Angle deviation response of the TCSC-PIDF controller using PIDF-EPSCA, PIDF-SCA, PIDF-MFO, and PIDF-EP techniques for Scenario A-1.

The speed deviation response for Scenario A-1 is shown in Figure 16. PIDF-EPSCA displayed an improvement in oscillatory mode responses, and speed deviation decayed earlier as compared to other standard methods. The proposed system took 1.35 s to decay speed deviation oscillations after the simulation started, followed by the PIDF-SCA, PIDF-MFO, and PIDF-EP methods, respectively. The PIDF-EP system was in the last position and took the longest of the four ways to dampen speed deviation swings. The damping time of all other techniques aside from PIDF-EPSCA was greater than two seconds.

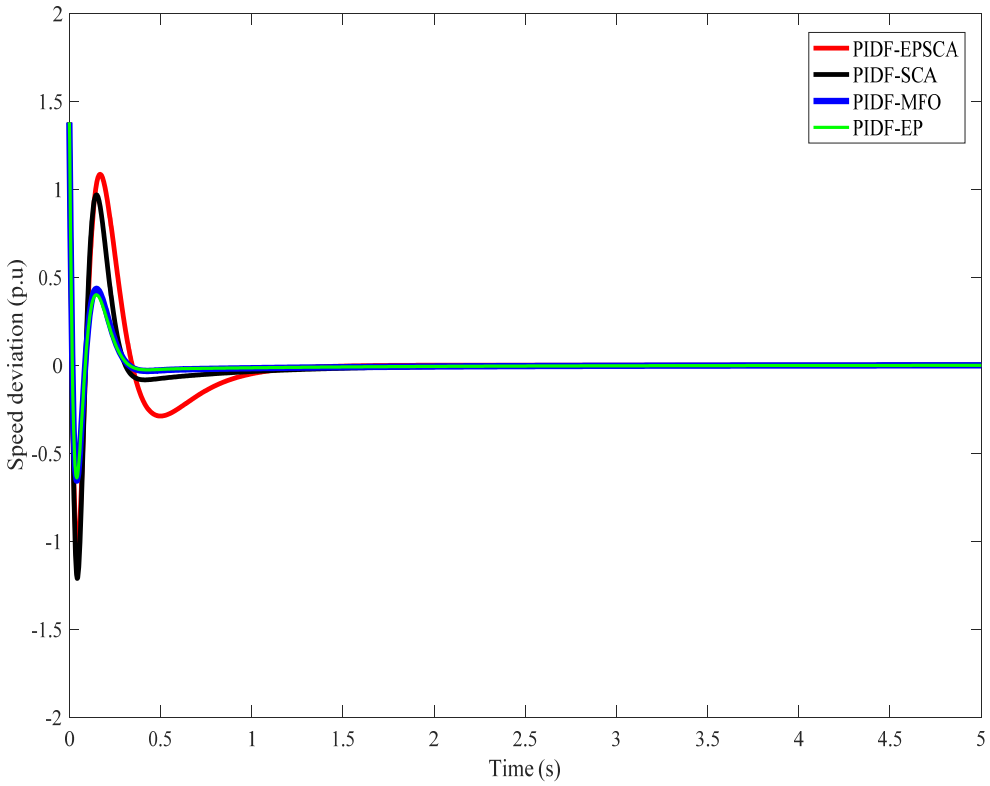


Figure 16. Speed deviation response of the TCSC-PIDF controller using PIDF-EPSCA, PIDF-SCA, PIDF-MFO, and PIDF-EP techniques for Scenario A-1.

An eigenvalue consists of a real part and an imaginary part. A stable system has a negative real part of its total eigenvalues. The imaginary axis line is a vertical line in the complex s-plane, where each point represents a complex number with zero real components (only the imaginary part) and, conversely, is a real axis line. A conjugate pair of eigenvalues with the imaginary part only (zero real part) represents the oscillation mode. A conjugate pair of eigenvalues with a negative real part and an imaginary part represent the decaying oscillation mode. An eigenvalue has only the negative real part with the zero imaginary part, which represents the exponential decay of the non-oscillation mode. The amplitude of the oscillation modes depends on the imaginary part of the eigenvalues and settling time depends on the real part of the eigenvalues. If one or more eigenvalues are located nearer to the imaginary axis line, then the amplitude of the oscillation modes is very high.

The Scenario A-1 eigenvalue sectors are displayed in Figure 17. Overall, all methods were successful in moving the eigenvalue location to the left side of the phase plan, indicating that all systems were stable. In this case, PIDF-EPSCA outperformed the other three strategies by allocating the majority of the eigenvalue locations to the far left. One of the eigenvalues from the other three mapping methods was placed closest to the origin. The coordinates, which were nearly at the same location from -0.6427 p.u to -0.5339 p.u on the real axis, were thought to be in a less stable condition than PIDF-EPSCA, which was at -0.6687 p.u. The output of PIDF-EPSCA further demonstrated that the eigenvalue sector was moved to the real–imaginary plane's nearest point towards the real-axis. The fact that the PIDF-MFO and PIDF-EP systems both had a pair of eigenvalues that were closest to the imaginary axis and furthest from the real axis, respectively, supports the notion that these two approaches were the worst. Thus, PIDF-EPSCA was confirmed as the suitable option for improving SMIB system stability.

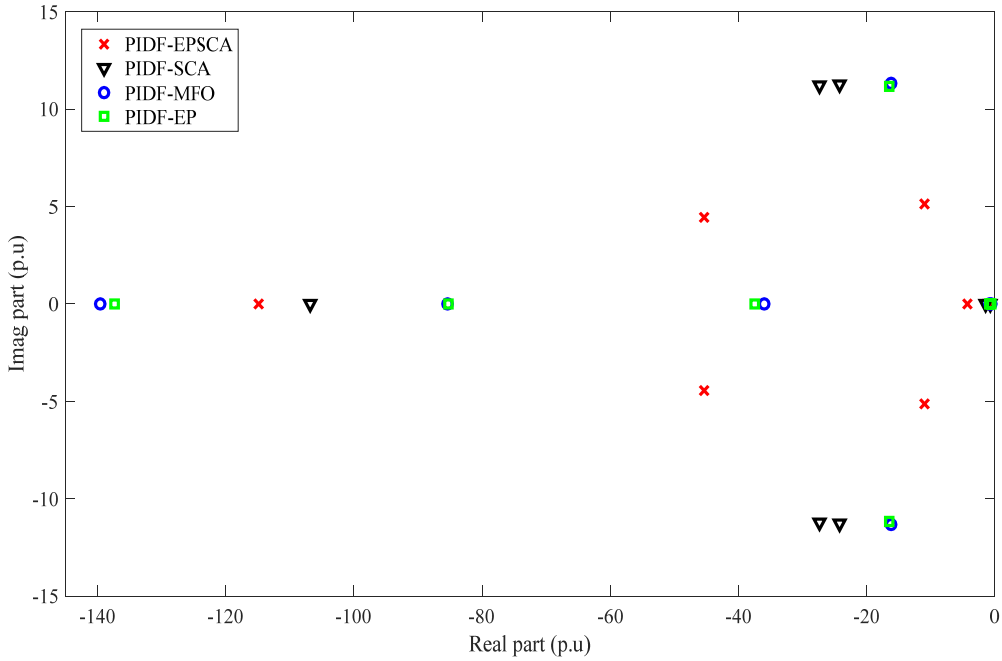


Figure 17. Eigenvalue distribution of the TCSC-PIDF controller system using PIDF-EPSCA, PIDF-SCA, PIDF-MFO, and PIDF-EP techniques for Scenario A-1.

Table 3 shows the N, K_P, K_D, and K_I parameters' objective functions, number of iterations, and settling times for the four optimisation techniques for Scenario A-1. In comparison to existing optimisation techniques, the suggested hybrid EPSCA strategy offered improved damping of angle deviation and eigenvalue location. In terms of eigenvalue location, the suggested EPSCA method offered a greater shift towards the real axis of the s-plane to reduce the abrupt variation in the amplitude of angle deviation and boosts system stability by moving the eigenvalues farther to the left of an imaginary axis line. In contrast to other optimisation techniques, the PIDF-EPSCA system needed nine iterations to converge the solution (Table 3). Unlike other optimisation techniques, the PIDF-SCA method needed 25 iterations to converge the maximum objective function (Table 3). The MFO and EP systems converged on the results after 60 and 10 iterations, respectively. The minimum objective function value of the PIDF-EP system resulted in a higher convergence rate. The suggested method had greater computing efficiency than the PIDF-EP system and provided a superior objective function than the three other techniques.

Table 3. Comparison of PIDF-EPSCA, PIDF-SCA, PIDF-MFO, and PIDF-EP for Scenario A-1.

Type	PIFF-EPSCA	PIDF-SCA	PIDF-MFO	PIDF-EP
Parameters optimised	K_P = 0.024275 K_D = 0.000531 K_I = 0.111213 N = 122.1625	K_P = 0.023936 K_D = 0.000318 K_I = 0.018067 N = 102.0015	K_P = 0.038666 K_D = 0.000202 K_I = 0.084392 N = 184.5104	K_P = 0.039688 K_D = 0.000169 K_I = 0.084817 N = 184.2895
Objective function value	0.1740 DR = 0.9041 DF = −0.6687	0.1338 DR = 0.9070 DF = −0.6427	0.1240 DR = 0.8179 DF = −0.5660	0.1253 DR = 0.8258 DF = −0.5339
No. of iterations	9	25	60	10
Settling time (s)	1.35	2	2.35	2.5

As a result, the suggested optimisation strategy, which uses MO as the objective function, was able to simultaneously improve both DF and DR by giving them equal weight in the development process for a system with improved damping capabilities. This

situation demonstrated how the suggested EPSCA technique can stabilise the signal in an SMIB power system and optimise the TCSC-PIDF controller values with a maximum objective function as the proposed MO function.

The angle deviation response for Scenario A-2 is shown in Figure 18. When compared with the other conditions, PIDF-EPSCA exhibited the smoothest response and shortest swing for angle deviation response. Within 1.1 s of the start of the simulation, the system was damped. The PIDF-SCA ranked second, followed by the PIDF-MFO and PIDF-EP. The PIDF-EP system was in the last position and took the longest to damp the oscillation. Other approaches, except PIDF-EPSCA, required damping times greater than 5 s.

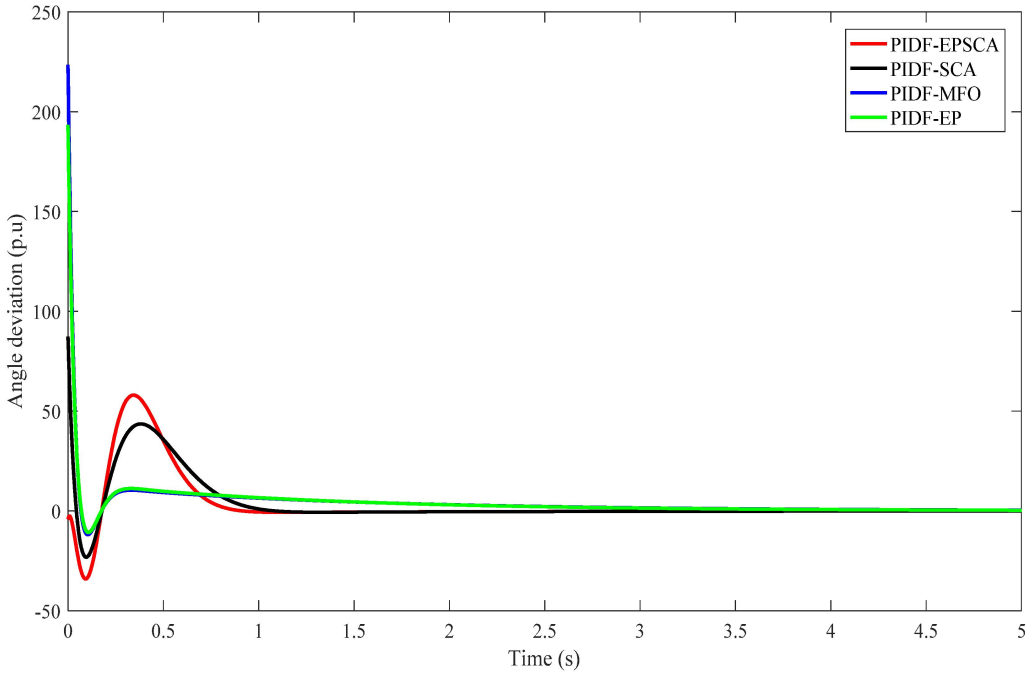


Figure 18. Angle deviation response of the TCSC-PIDF controller using PIDF-EPSCA, PIDF-SCA, PIDF-MFO, and PIDF-EP techniques for Scenario A-2.

Figure 19 depicts the Scenario A-2 speed deviation effect. In comparison to other conventional approaches, PIDF-EPSCA showed an improvement in oscillatory mode responses, and speed deviation decayed earlier. After the simulation began, the suggested system took 1.1 s to decay the speed deviation oscillations, followed by the PIDF-SCA, PIDF-MFO, and PIDF-EP approaches, in that order. The final and slowest of the four methods to soften speed deviation swings was the PIDF-EP system. All other methods except PIDF-EPSCA had damping times that were longer than five seconds.

The eigenvalue sectors for Scenario A-2 are displayed in Figure 20. Overall, all methods succeeded in moving the eigenvalue location to the left side of the phase plan, demonstrating the stability of all systems. When compared with the other three strategies, PIDF-EPSCA was able to allocate the majority of the eigenvalue locations further to the left. The closest point to the origin was where one of the eigenvalues of the other three approaches was mapped. In comparison to PIDF-EPSCA, which was at -0.6242 p.u on the real axis, the coordinates, which were nearly at the same point between -0.6227 p.u to -0.5176 p.u, were assumed to be in a less stable condition. The output of PIDF-EPSCA further demonstrated that the eigenvalue sector was moved to the real–imaginary plane's nearest point towards the real axis. The fact that the PIDF-MFO and PIDF-EP systems both had a pair of eigenvalues that were closest to the imaginary axis and furthest from the real axis, respectively, supports the notion that these two approaches were the worst. Thus, PIDF-EPSCA was validated as the top option for improving SMIB system stability.

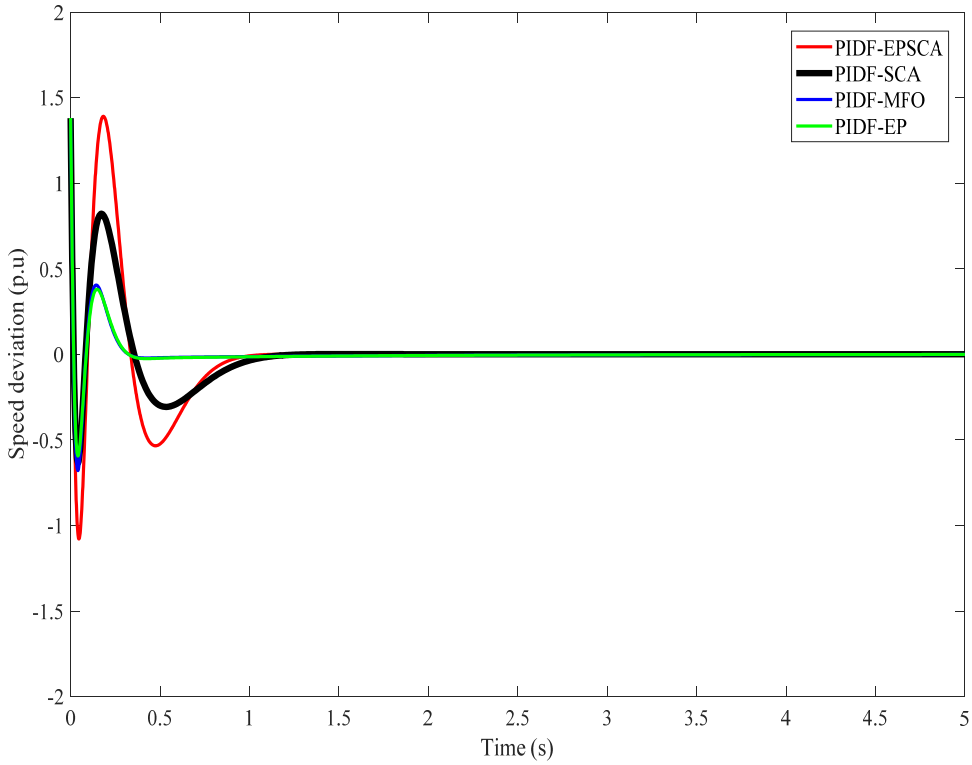


Figure 19. Speed deviation response of TCSC-PIDF controller using PIDF-EPSCA, PIDF-SCA, PIDF-MFO, and PIDF-EP techniques for Scenario A-2.

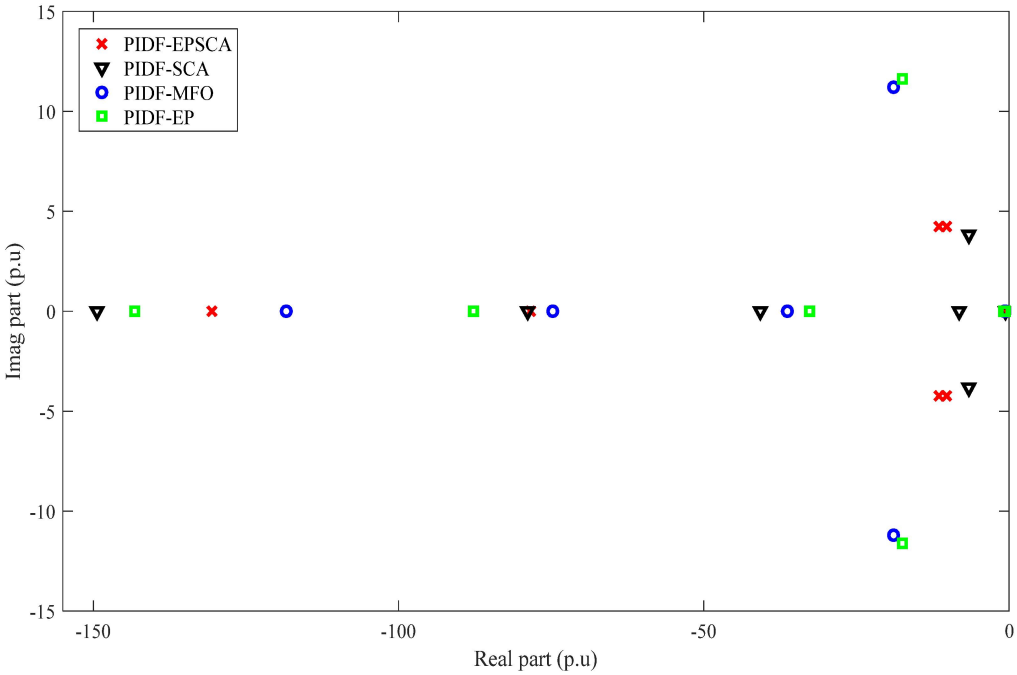


Figure 20. Eigenvalue distribution of TCSC-PIDF controller system using PIDF-EPSCA, PIDF-SCA, PIDF-MFO, and PIDF-EP techniques for Scenario A-2.

Table 4 lists the four optimisation techniques' parameters' (N, K_P, K_D, and K_I) objective functions, iterations, and settling times for Scenario A-2. In comparison to existing optimisation techniques, the suggested hybrid EPSCA strategy offers improved damping of angle deviation and eigenvalue location. In terms of eigenvalue location, the suggested EPSCA

method offered a greater shift towards the real axis of the s-plane to reduce the abrupt variation in the amplitude of angle deviation and boosted system stability by moving the eigenvalues farther to the left of an imaginary axis line. Unlike other optimisation techniques, the PIDF-EPSCA system needed 13 iterations to converge the solution (Table 4). In contrast to other optimisation techniques, the PIDF-SCA system needed 32 iterations to converge the maximum objective function (Table 4). The MFO and EP systems converged on the results after 52 and 6 iterations, respectively. The minimal objective function value of the PIDF-EP system resulted in a higher convergence rate. The suggested method offered better computing efficiency than the PIDF-EP system and a superior objective function than the three other techniques.

Table 4. Comparison of PIDF-EPSCA, PIDF-SCA, PIDF-MFO, and PIDF-EP for Scenario A-2.

Type	PIDF-EPSCA	PIDF-SCA	PIDF-MFO	PIDF-EP
Parameters optimised	K_P = 0.020772 K_D = 0.000686 K_I = 0.0892724 N = 142.90544	K_P = 0.033540 K_D = 0.000612 K_I = 0.216218 N = 180.87885	K_P = 0.039233 K_D = 0.000148 K_I = 0.0694360 N = 158.67512	K_P = 0.040951 K_D = 0.000198 K_I = 0.0894365 N = 189.86943
Objective function value	0.1895 DR = 0.9221 DF = −0.6242	0.1915 DR = 0.8635 DF = −0.6227	0.1289 DR = 0.8613 DF = −0.5176	0.1244 DR = 0.8258 DF = −0.5339
No. of iterations	13	32	52	6
Settling time (s)	1.1	1.16	5	4.35

As a result, the suggested optimisation strategy, which used MO as the objective function, was able to simultaneously improve DF and DR by giving them equal weight in the development process for a system with improved damping capabilities. This demonstrated how the suggested EPSCA technique can stabilise the signal in an SMIB power system and optimise the TCSC-PIDF controller parameters with a maximum objective function as the proposed MO function.

The response to the angle deviation in Scenario A-3 is shown in Figure 21. In terms of responsiveness to angle variation, PIDF-EPSCA had the smoothest response and the least swing when compared with the other methods. After the simulation began, the system was damped in 1.47 s. Following PIDF-MFO and PIDF-EP, PIDF-SCA came in second. The PIDF-EP system was in the final position and took the longest time to dampen the oscillation out of the four strategies. Other approaches, apart from PIDF-EPSCA, had damping times longer than 3.9 s.

The Scenario A-3 speed deviation effect is shown in Figure 22. PIDF-EPSCA displayed an improvement in oscillatory mode responses, and speed deviation decayed earlier as compared to other conventional techniques. The simulation showed that the proposed system, followed in that order by the PIDF-SCA, PIDF-MFO, and PIDF-EP techniques, took 1.47 s to decay speed deviation oscillations. The PIDF-EP system was the fourth and slowest way to smooth speed deviation fluctuations. Except for PIDF-EPSCA, all other techniques had damping times that were greater than 3.9 s.

The Scenario A-3 eigenvalue sectors are displayed in Figure 23. Overall, all methods were successful in moving the eigenvalue location to the left side of the phase plan, indicating that all systems were stable. In this case, PIDF-EPSCA outperformed the other three strategies by allocating the majority of the eigenvalue locations to the far left. One of the eigenvalues from the other three mapping methods was placed closest to the origin. The coordinates, which were nearly at the same point from −0.4760 p.u to −0.4543 p.u on the real axis, were thought to be in a less stable condition than PIDF-EPSCA, which was at −0.4765 p.u on the real axis. The PIDF-EPSCA result also demonstrated that the eigenvalue sector had been moved to the closest position to the real axis of the real–imaginary plane. One set of eigenvalues for the PIDF-MFO and PIDF-EP systems was situated in positions

that were farthest from the real axis and closest to the imaginary axis, respectively. This finding indicates that these two approaches were the poorest ones. Thus, the optimum option for improving SMIB system stability is PIDF-EPSCA.

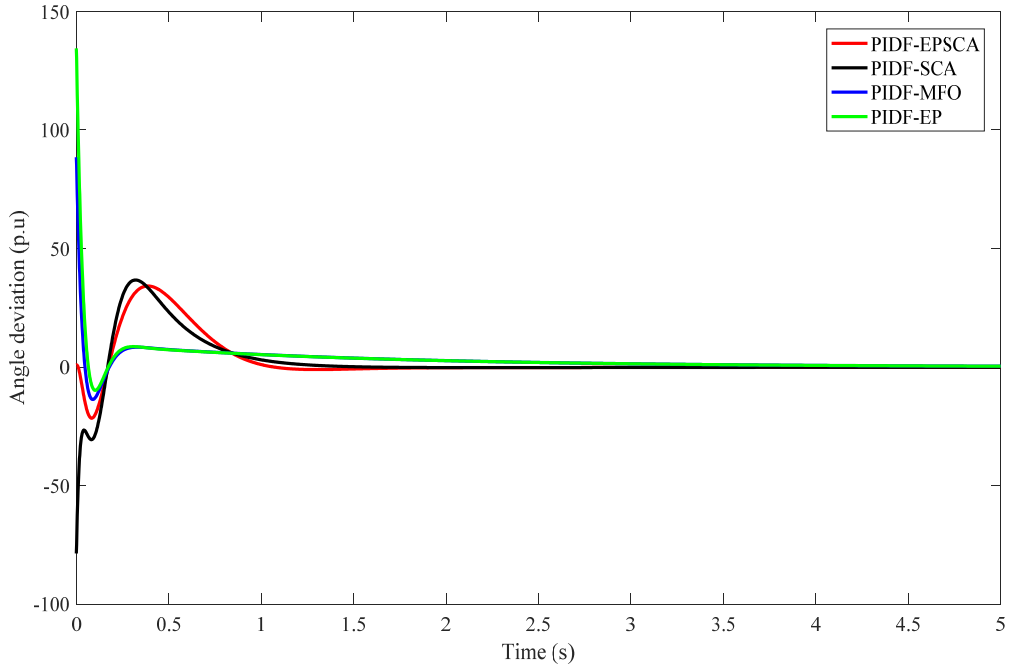


Figure 21. Angle deviation response of the TCSC-PIDF controller using PIDF-EPSCA, PIDF-SCA, PIDF-MFO, and PIDF-EP techniques for Scenario A-3.

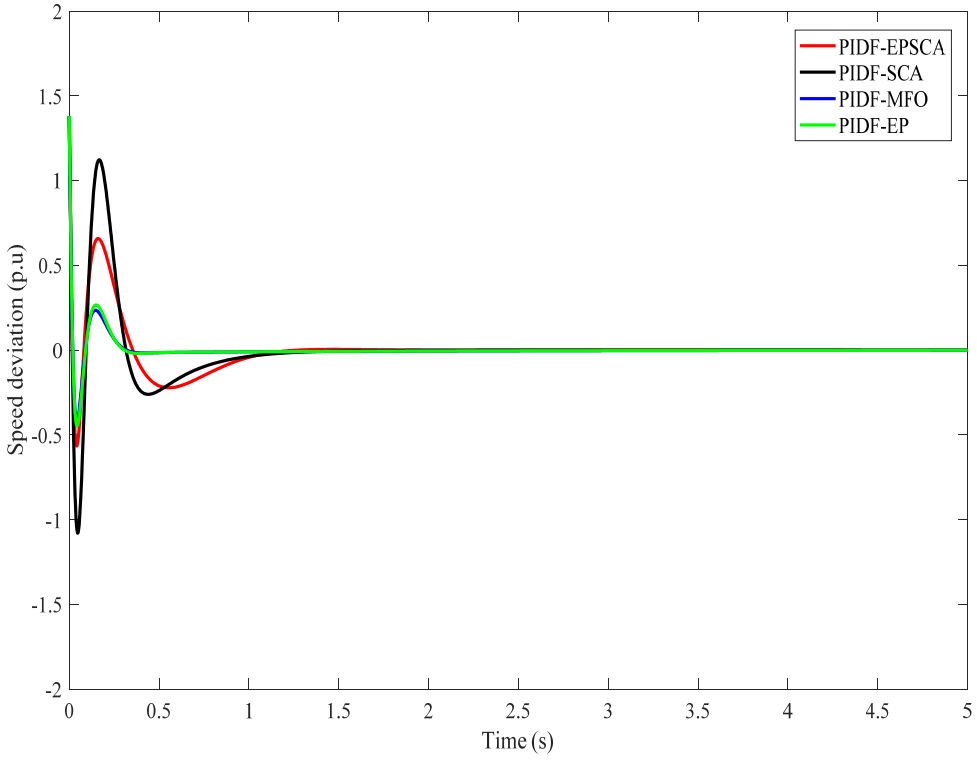


Figure 22. Speed deviation response of the TCSC-PIDF controller using PIDF-EPSCA, PIDF-SCA, PIDF-MFO, and PIDF-EP techniques for Scenario A-3.

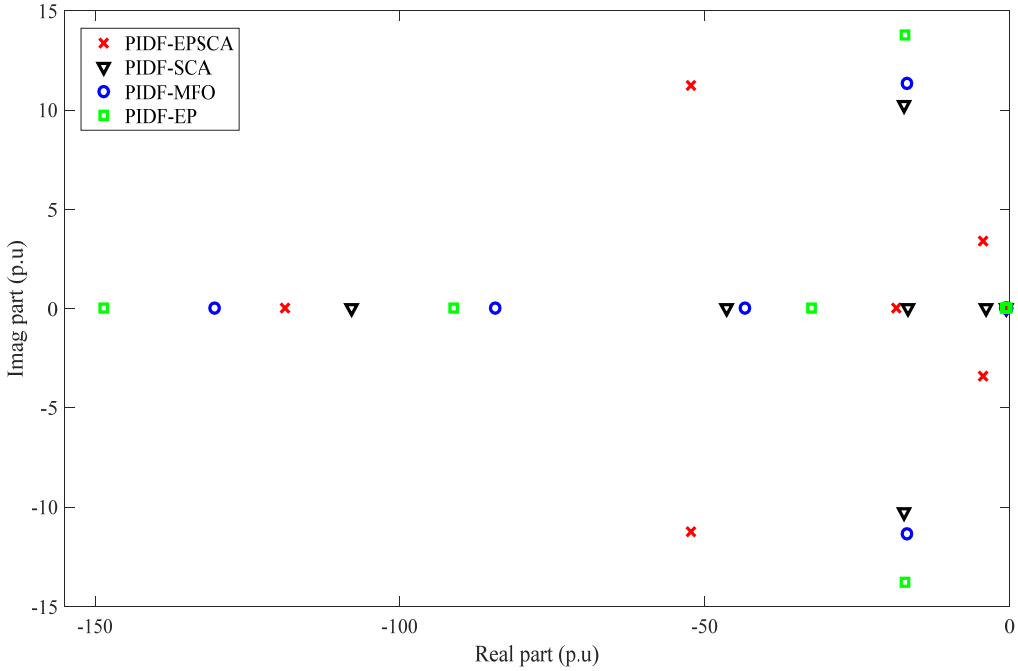


Figure 23. Eigenvalue distribution of TCSC-PIDF controller system using PIDF-EPSCA, PIDF-SCA, PIDF-MFO, and PIDF-EP techniques for Scenario A-3.

The parameters' (N, K_P, K_D, and K_I) objective functions, iterations, and settling times for the four optimisation approaches are shown in Table 5 for Scenario A-3. When compared with existing optimisation techniques, the proposed hybrid EPSCA strategy offered greater damping of angle deviation and eigenvalue location. The suggested EPSCA algorithm shifted eigenvalues closer to the left of an arbitrary axis line, which improved system stability while reducing the abrupt variation in angle deviation amplitude. Compared with other optimisation methods, the PIDF-EPSCA system needed 12 iterations to converge the solution (Table 5). The PIDF-SCA system, in contrast to previous optimisation techniques, needed 32 iterations to converge the maximum objective function (Table 5). The MFO and EP systems required 62 and 7 iterations, respectively, to converge on the results. With the lowest objective function value, the PIDF-EP system had a higher rate of convergence. In comparison to the three other techniques, the proposed technique provided a superior objective function and was as computationally efficient as the PIDF-EP system.

Therefore, the suggested optimisation strategy can be used to improve the system's performance when MO is used as the objective function. This improvement may be achieved by providing similar weights to DF and DR to increase the system's damping capacity. This finding demonstrates that the suggested EPSCA technique can stabilise the signal in an SMIB power system and optimise the TCSC-PIDF controller variables with a maximum objective function as the provided MO function.

The angle deviation response for Scenario A-4 is shown in Figure 24. PIDF-EPSCA exhibited the smoothest response and the smallest swing for angle deviation response when compared with the other methods. Following the start of the simulation, the system was damped in 0.95 s. PIDF-SCA ranked second followed by PIDF-MFO and PIDF-EP, respectively. The PIDF-EP system ranked last among the four strategies and took the longest time to damp the oscillation. All other approaches except PIDF-EPSCA needed longer than 3.5 s to damp the oscillation.

Table 5. Comparison of PIDF-EPSCA, PIDF-SCA, PIDF-MFO, and PIDF-EP for Scenario A-3.

Type	PIDF-EPSCA	PIDF-SCA	PIDF-MFO	PIDF-EP
Parameters optimised	K_P = 0.011841 K_D = 0.000825 K_I = 0.004116 N = 77.39919	K_P = 0.020819 K_D = 0.000705 K_I = 0.070581 N = 100.06704	K_P = 0.050461 K_D = 0.000182 K_I = 0.0815191 N = 182.95746	K_P = 0.048138 K_D = 0.000213 K_I = 0.025814 N = 197.6818
Objective function value	0.1240 DR = 0.8596 DF = −0.4765	0.1221 DR = 0.8600 DF = −0.4760	0.1247 DR = 0.8282 DF = −0.4543	0.1244 DR = 0.8258 DF = −0.5339
No. of iterations	12	32	62	7
Settling time (s)	1.47	1.7	5	3.9

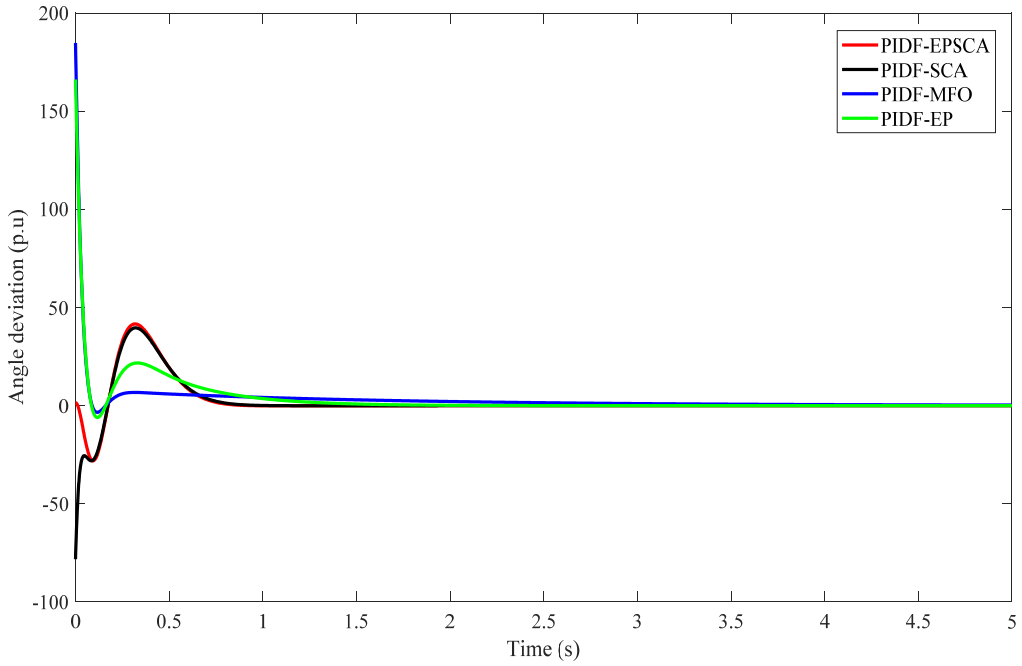


Figure 24. Angle deviation response of the TCSC-PIDF controller using PIDF-EPSCA, PIDF-SCA, PIDF-MFO, and PIDF-EP techniques for Scenario A-4.

Figure 25 depicts the Scenario A-4 speed deviation effect. In comparison to other standard approaches, PIDF-EPSCA showed an improvement in oscillatory mode response and speed deviation decayed response. The simulation demonstrated that the suggested system took 0.95 s to decay speed deviation oscillations, followed by the PIDF-SCA, PIDF-MFO, and PIDF-EP approaches, respectively. The fourth and slowest method for reducing speed deviation fluctuations was the PIDF-EP system. All other approaches had damping times that were longer than 3.5 s, apart from PIDF-EPSCA.

The eigenvalue sector for Scenario A-4 is shown in Figure 26. Overall, all strategies were successful in moving the eigenvalue location to the phase plan's left side, indicating that all systems were stable. PIDF-EPSCA, in contrast to the other three strategies, was able to allocate the majority of the eigenvalue location on the far-left side of the imaginary axis. The eigenvalue that was mapped closest to the origin by the other three methods was each of theirs. When compared with PIDF-EPSCA, which was at −0.276312 p.u on the real axis, the coordinates, which were practically at the same location from −0.27630 p.u to −0.27560 p.u, were thought to be in a less stable situation. The output of PIDF-EPSCA demonstrated that the eigenvalue sector was moved to the real–imaginary plane's closest point to the real axis. The fact that the PIDF-MFO and PIDF-EP systems both pairs of

eigenvalues situated farthest from the real axis and closer to the imaginary axis supports the claim that these two approaches were the worst-performing ones. Thus, PIDF-EPSCA is the optimal method for enhancing SMIB system stability.

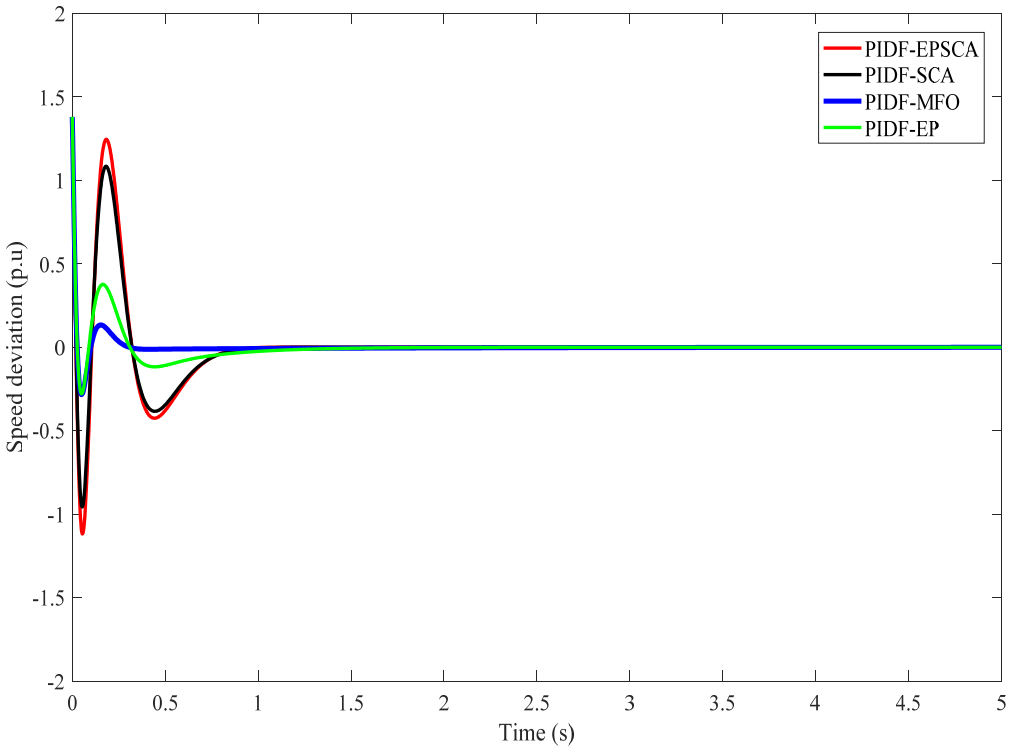


Figure 25. Speed deviation response of the TCSC-PIDF controller using PIDF-EPSCA, PIDF-SCA, PIDF-MFO, and PIDF-EP techniques for Scenario A-4.

The parameters' (K_P, K_D, N, and K_I) objective functions, iterations, and settling times for Scenario A-4 are shown in Table 6. The suggested hybrid EPSCA strategy offered better angle deviation damping and eigenvalue location than existing optimisation techniques. The suggested EPSCA algorithm shifted eigenvalues closer to the left of an arbitrary axis line to enhance system stability while limiting abrupt changes in angle deviation amplitude. Unlike other optimisation techniques, the PIDF-EPSCA system took 14 iterations to converge the solution (Table 6). To converge the maximal objective function, the PIDF-SCA system needed 42 iterations, whereas the other optimisation techniques needed only one iteration (Table 6). The MFO and EP systems took 49 and 8 iterations, respectively, to converge on the results. The PIDF-EP system had a higher rate of convergence with lower objective function values. The proposed technique had a superior objective function and a higher computing efficiency than the three other techniques and the PIDF-EP system.

Therefore, the suggested optimisation technique, which uses MO as the objective function, can be used to optimise the system's performance while simultaneously improving the damping DR and the DF. This ability demonstrates how the suggested EPSCA technique may adjust the TCSC-PIDF controller parameters by using a maximum objective function as the proposed MO function and stabilise the signal in an SMIB power system.

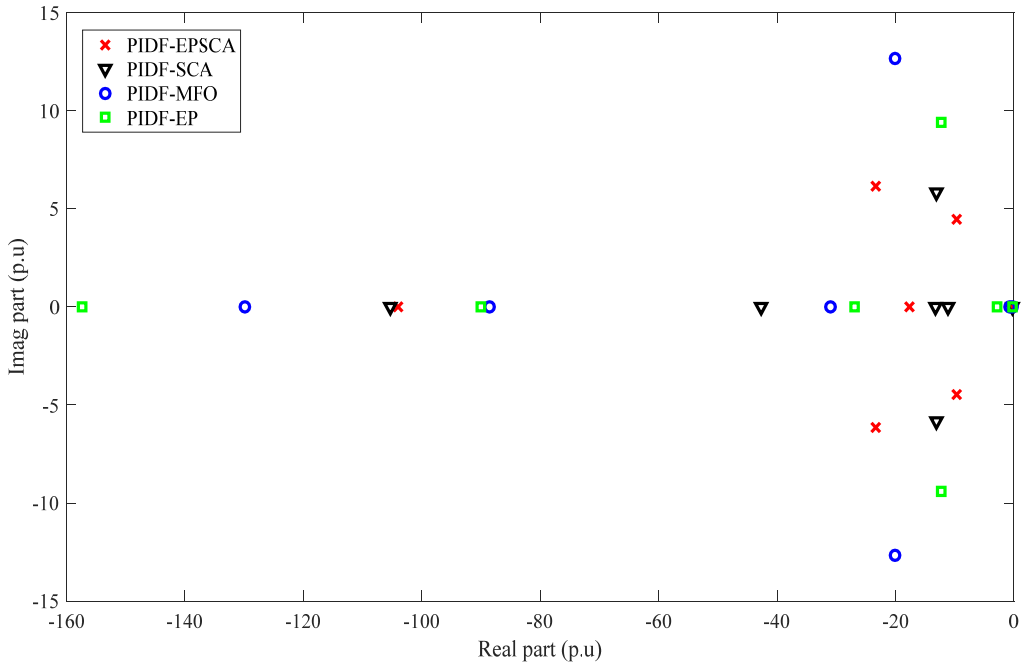


Figure 26. Eigenvalue distribution of the TCSC-PIDF controller system using PIDF-EPSCA, PIDF-SCA, PIDF-MFO, and PIDF-EP techniques for Scenario A-4.

Table 6. Comparison of PDF-EPSCA, PIDF-SCA, PIDF-MFO, and PIDF-EP for Scenario A-4.

Type	PIDF-EPSCA	PIDF-SCA	PIDF-MFO	PIDF-EP
Parameters optimised	K_P = 0.013117 K_D = 0.001151 K_I = 0.007107 N = 77.75017	K_P = 0.018126 K_D = 0.001107 K_I = 0.057536 N = 88.88804	K_P = 0.062337 K_D = 0.000297 K_I = 0.0859279 N = 180.39036	K_P = 0.048779 K_D = 0.000879 K_I = 0.2615544 N = 192.05312
Objective function value	0.1615 DR = 0.9069 DF = −0.276312	0.1625 DR = 0.9126 DF = −0.276305	0.1220 DR = 0.8457 DF = −0.275601	0.1282 DR = 0.7947 DF = −0.27621
No. of iterations	14	42	49	8
Settling time (s)	0.95	1.05	3.5	2.1

5. Discussion

The main objective of this research is to develop a robust damping controller that dampens the low frequency oscillations in a power system. This is done by developing a mathematical model of a PIDF controller and its modelling with a FACTS-based damping scheme (TCSC), an objective function, and an optimization algorithm. The results section of this article shows that proposed EPSCA optimized all the parameters of the PIDF controller using the proposed multi objective function, and it linearized the nonlinear PIDF-TCSC system and eigenvalue analysis method to dampen the low frequency oscillations as compared to standard algorithms. This was tested with four different loading conditions.

The hybrid EPSCA technique combines the features of SCA and EP techniques. Figure 6 show both the SCA section and the EP section in the flow chart of the EPSCA technique. The first half and second half iterations of the SCA allow for exploration and exploitation in a search space, respectively. This technique differs from other algorithms due to this capability. When exploring search space and using the eigenvalue analysis to locate maxima or minima, SCA optimisation generally yields superior results. The search exploitation strategy for quick convergence has the only restriction with SCA. For a system that needs a lot of parameters to optimise, the SCA optimization process requires a lot of

time to produce quality solutions, and it has limitations with consistent solutions. The solution inconsistency of the SCA is due to its low convergence rate. The cure of this pitfall of SCA is the hybrid EPSCA, which utilises the best features of EP, which has high convergence rate and delivers solution performance by raising its convergence rate and solution consistency and is a modified form of SCA.

The results of the TCSC-PIDF controller system's angle deviation responses, speed deviation responses, and eigenvalue distributions using the EPSCA technique under various loading conditions demonstrate that the suggested optimisation strategy offers a system that enhances the damping capabilities by using the proposed multi objective function. By assigning both DF and DR equal weight during the optimization process, MO, the objective function, is able to simultaneously enhance both DF and DR metrics. In contrast to conventional methods, the results illustrate how the recommended EPSCA strategy may stabilise the signal in an SMIB power system and optimise the TCSC-PIDF controller parameter settings with maximum objective function values and a high convergence rate.

6. Conclusions

This research introduced the effective design of damping controllers to safeguard the stability of a single-machine infinite-bus system to control rising low-frequency oscillations in power systems. This research designed a robust damping controller by developing a model of the PIDF controller, discovering a good objective function and developing an efficient EPSCA optimisation technique. The major contributions of this research and constraints of this study are presented.

To accomplish this research, the developed hybrid EPSCA optimisation technique was achieved based on the concept of mutation. The concept of mutation was implemented by modifying the existing features of the SCA technique. The concept of mutation by the Levy flight algorithm was used to improve the specific search exploitation strategy of SCA for solution consistency and a high convergence rate. The proposed algorithm provides good solution performance in exploration and exploitation processes for rapid and consistent convergence to find the maxima or minima in eigenvalue analysis. The EPSCA design-based PIDF damping controller showed significant improvements in settling times and overshoots of different low-frequency oscillation modes compared with SCA, MFO, and EP techniques. The performance of EPSCA was verified on an SMIB system with an MO function. The enhanced search ability of EPSCA was assessed versus that of SCA, MFO, and EP in terms of solution precision, reliability, and convergence rate.

Author Contributions: Conceptualisation, A.W.K. and N.A.M.K.; methodology, A.W.K. and N.A.M.K.; software, A.W.K.; validation, A.W.K. and N.A.M.K.; formal analysis, A.W.K.; investigation, A.W.K.; resources, A.W.K. and N.A.M.K.; data curation, A.W.K.; writing—original draft preparation, A.W.K.; writing—review and editing, A.W.K., N.A.M.K., M.A.A.M.Z., and M.H.M.Z.; visualisation, A.W.K. and N.A.M.K.; supervision, N.A.M.K. and M.A.A.M.Z.; project administration, A.W.K. and N.A.M.K.; funding acquisition, N.A.M.K., M.A.Z., and I.M. All authors have read and agreed to the published version of the manuscript.

Funding: The authors appreciate the support given by the Ministry of Higher Education and the Universiti Kebangsaan Malaysia for the operational and financial support to this project under Project Codes GUP-2020-018 and RHB-UKM-2021-002.

Institutional Review Board Statement: Not applicable.

Informed Consent Statement: Not applicable.

Data Availability Statement: Not applicable.

Conflicts of Interest: The authors declare no conflict of interest.

References

1. Kundur, P. *Power System Stability Controls*, 3rd ed.; McGraw-Hill: New York, NY, USA, 1994; pp. 17–817.
2. Wang, H.; Du, W. *Analysis and Damping Control of Power System Low-Frequency Oscillations*, 1st ed.; Springer: New York, NY, USA, 2016; pp. 1–182.
3. Anderson, P.; Fouad, A. *Power System Control and Stability*, 2nd ed.; Wiley-IEEE Press: Danvers, IL, USA, 2002; pp. 13–165.
4. Machowski, J.; Bialek, J.W.; Bumby, J.R. *Power System Dynamics: Stability and Control*, 2nd ed.; John Wiley & Sons Ltd.: Chichester, UK, 2008; pp. 159–271.
5. Hannan, M.A.; Islam, N.N.; Mohamed, A.; Lipu, M.S.H.; Ker, P.J.; Rashid, M.M.; Shareef, H. Artificial Intelligent Based Damping Controller Optimization for the Multi-Machine Power System: A Review. *IEEE Access* **2018**, *6*, 39574–39594. [CrossRef]
6. Ordóñez, C.A.; Gómez-Expósito, A.; Maza-Ortega, J.M. Series Compensation of Transmission Systems: A Literature Survey. *Energies* **2021**, *14*, 1717. [CrossRef]
7. Quan, W.; Su, Q. Improved Adaptive Backstepping Approach on STATCOM Controller of Nonlinear Power Systems. *IEEE Access* **2019**, *7*, 139109–139117. [CrossRef]
8. Guesmi, T.; Alshammari, B.M.; Almalaq, Y.; Alateeq, A.; Alqunun, K. New Coordinated Tuning of SVC and PSSs in Multimachine Power System Using Coyote Optimization Algorithm. *Sustainability* **2021**, *13*, 3131. [CrossRef]
9. AL Ahmad, A.; Sirjani, R. Optimal placement and sizing of multi-type FACTS devices in power systems using metaheuristic optimisation techniques: An updated review. *Ain Shams Eng. J.* **2019**, *11*, 611–628. [CrossRef]
10. Jiang, S.; Gole, A.M.; Annakkage, U.D.; Jacobson, D.A. Damping Performance Analysis of IPFC and UPFC Controllers Using Validated Small-Signal Models. *IEEE Trans. Power Deliv.* **2011**, *26*, 446–454. [CrossRef]
11. Zhou, L.; Swain, A.; Ukil, A. Reinforcement Learning Controllers for Enhancement of Low Voltage Ride through Capability in Hybrid Power Systems. *IEEE Trans. Ind. Inform.* **2020**, *16*, 5023–5031. [CrossRef]
12. Zuo, J.; Li, Y.; Shi, D.; Duan, X. Simultaneous Robust Coordinated Damping Control of Power System Stabilizers (PSSs), Static Var Compensator (SVC) and Doubly-Fed Induction Generator Power Oscillation Dampers (DFIG PODs) in Multimachine Power Systems. *Energies* **2017**, *10*, 565. [CrossRef]
13. Abido, M.A. A novel approach to conventional power system stabilizer design using tabu search. *Fuel Energy Abstr.* **1999**, *41*, 153. [CrossRef]
14. Ali, E.S. Optimization of Power System Stabilizers using BAT search algorithm. *Int. J. Electr. Power Energy Syst.* **2014**, *61*, 683–690. [CrossRef]
15. Jiang, P.; Fan, Z.; Feng, S.; Wu, X.; Cai, H.; Xie, Z. Mitigation of power system forced oscillations based on unified power flow controller. *J. Mod. Power Syst. Clean Energy* **2018**, *7*, 99–112. [CrossRef]
16. Al-Ismail, F.S.; Hassan, M.A.; Abido, M.A. RTDS Implementation of STATCOM-Based Power System Stabilizers. *Can. J. Electr. Comput. Eng.* **2014**, *37*, 48–56. [CrossRef]
17. Cai, L.-J.; Erlich, I. Simultaneous Coordinated Tuning of PSS and FACTS Damping Controllers in Large Power Systems. *IEEE Trans. Power Syst.* **2005**, *20*, 294–300. [CrossRef]
18. Eslami, M.; Babaei, B.; Shareef, H.; Khajehzadeh, M.; Arandian, B. Optimum Design of Damping Controllers Using Modified Sperm Swarm Optimization. *IEEE Access* **2021**, *9*, 145592–145604. [CrossRef]
19. Kamari, N.A.M.; Musirin, I.; Ibrahim, A.A. Swarm Intelligence Approach for Angle Stability Improvement of PSS and SVC-Based SMIB. *J. Electr. Eng. Technol.* **2020**, *15*, 1001–1014. [CrossRef]
20. Linda, M.M.; Nair, N.K. A new-fangled adaptive mutation breeder genetic optimization of global multi-machine power system stabilizer. *Int. J. Electr. Power Energy Syst.* **2013**, *44*, 249–258. [CrossRef]
21. Keskes, S.; Salleem, S.; Chrifi-Alaoui, L.; Kammoun, M.B.A. Nonlinear Coordinated Passivation Control of Single Machine Infinite Bus Power System with Static Var Compensator. *J. Mod. Power Syst. Clean Energy* **2021**, *9*, 1557–1565. [CrossRef]
22. Khawaja, A.W.; Kamari, N.A.M.; Zainuri, M.A.A.M. Design of a Damping Controller Using a Metaheuristic Algorithm for Angle Stability Improvement of an MIB System. *Appl. Sci.* **2022**, *12*, 589. [CrossRef]
23. Khawaja, A.W.; Kamari, N.A.M.; Musirin, I.; Zulkifley, M.A.; Sujod, M.Z. Design of optimal multi-objective-based facts component with proportional-integral-derivative controller using swarm optimization approach. *Int. J. Adv. Technol. Eng. Explor.* **2021**, *8*, 391–404. [CrossRef]
24. Khawaja, A.W.; Kamari, N.A.M.; Zainuri, M.A.A.M. Design of a Damping Controller Using the SCA Optimization Technique for the Improvement of Small Signal Stability of a Single Machine Connected to an Infinite Bus System. *Energies* **2021**, *14*, 2996. [CrossRef]
25. Sambariya, D.K.; Prasad, R. Robust tuning of power system stabilizer for small signal stability enhancement using metaheuristic bat algorithm. *Int. J. Electr. Power Energy Syst.* **2014**, *61*, 229–238. [CrossRef]
26. Yakout, A.; Sabry, W.; Hasanien, H.M. Enhancing rotor angle stability of power systems using marine predator algorithm based cascaded PID control. *Ain Shams Eng. J.* **2021**, *12*, 1849–1857. [CrossRef]
27. Jahanshahi, E.; Oliveira, V.D.; Grimholt, C.; Skogestad, S. A comparison between Internal Model Control, optimal PIDF and robust controllers for unstable flow in risers. *IFAC* **2014**, *47*, 5752–5759. [CrossRef]
28. Sahu, R.K.; Sekhar, G.T.C.; Panda, S. DE optimized fuzzy PID controller with derivative filter for LFC of multi source power system in deregulated environment. *Ain Shams Eng. J.* **2015**, *2*, 511–530. [CrossRef]

29. Cuoghi, S.; Ntogramatzidis, L.; Padula, F.; Grandi, G. Direct Digital Design of PIDF Controllers with ComPlex Zeros for DC-DC Buck Converters. *Energies* **2019**, *12*, 36. [CrossRef]
30. Yakout, A.H.; Kotb, H.; Hasanien, H.M.; Aboras, K.M. Optimal Fuzzy PIDF Load Frequency Controller for Hybrid Microgrid System Using Marine Predator Algorithm. *IEEE Access* **2021**, *9*, 54220–54232. [CrossRef]
31. Hassan, M.; Abido, M.A.; Aliyu, A. Design of Power System Stabilizer Using Phase Based Objective Function and Heuristic Algorithm. In Proceedings of the 2019 8th International Conference on Modeling Simulation and Applied Optimization (ICMSAO), Manama, Bahrain, 15–17 April 2019; IEEE: New York, NY, USA, 2019. [CrossRef]
32. Paital, S.R.; Ray, P.K.; Mohanty, A.; Patra, S.; Dubey, H. Bacterial Foraging Optimized STATCOM for Stability Assessment in Power System. In Proceedings of the 2016 IEEE Students' Technology Symposium(TechSym), Kharagpur, India, 30 September–2 October 2016; IEEE: New York, NY, USA, 2019; pp. 85–89. [CrossRef]
33. Shankar, R.; Bhushan, R.; Chatterjee, K. Small-signal stability analysis for two-area interconnected power system with load frequency controller in coordination with FACTS and energy storage device. *Ain Shams Eng. J.* **2016**, *7*, 603–612. [CrossRef]
34. Chaib, L.; Choucha, A.; Arif, S. Optimal design and tuning of novel fractional order PID power system stabilizer using a new metaheuristic Bat algorithm. *Ain Shams Eng. J.* **2017**, *8*, 113–125. [CrossRef]
35. Dasu, B.; Kumar, M.S.; Rao, R.S. Design of robust modified power system stabilizer for dynamic stability improvement using Particle Swarm Optimization technique. *Ain Shams Eng. J.* **2019**, *10*, 769–783. [CrossRef]
36. Guchhait, P.K.; Banerjee, A.; Mukherjee, V. Comparative study using soft computing techniques for the reactive power compensation of a hybrid power system model. *Ain Shams Eng. J.* **2019**, *11*, 87–98. [CrossRef]
37. Banaei, M.R.; Seyed-Shenava, S.J.; Farahbakhsh, P. Dynamic stability enhancement of power system based on a typical unified power flow controllers using imperialist competitive algorithm. *Ain Shams Eng. J.* **2014**, *5*, 691–702. [CrossRef]
38. Morsali, J.; Zare, K.; Hagh, M.T. Performance comparison of TCSC with TCPS and SSSC controllers in AGC of realistic interconnected multi-source power system. *Ain Shams Eng. J.* **2016**, *7*, 143–158. [CrossRef]
39. Panda, S.; Padhy, N.P. Application of genetic algorithm for pss and facts-based controller design. *Int. J. Comput. Methods* **2008**, *5*, 607–620. [CrossRef]
40. Li, C.; Deng, J.; Zhang, X. Coordinated design and application of robust damping controllers for shunt FACTS devices to enhance small-signal stability of large-scale power systems. *CSEE J. Power Energy Syst.* **2017**, *3*, 399–407. [CrossRef]
41. Kamari, N.A.M.; Musirin, I.; Ibrahim, A.A.; Halim, S.A. Intelligent swarm-based optimization technique for oscillatory stability assessment in power system. *IAES Int. J. Artif. Intell.* **2019**, *8*, 342–351. [CrossRef]
42. Mirjalili, S. SCA: A Sine Cosine Algorithm for solving optimization problems. *Knowl. Based Syst.* **2016**, *96*, 120–133. [CrossRef]
43. Mirjalili, S. Moth-flame optimization algorithm: A novel nature-inspired heuristic paradigm. *Knowl. Based Syst.* **2015**, *89*, 228–249. [CrossRef]
44. Kamari, N.A.M.; Musirin, I.; Othman, M.M. IPSO based SVC-PID for angle stability enhancement. *Int. J. Simul. Syst. Sci. Technol.* **2016**, *17*, 20.1–20.7. [CrossRef]